Y210504

Stress Migration Failure Analysis of Aluminium Line of a Multilevel Printed Circuit Board using Boundary Element Method

By

Ankit Kumar Garg

Th
ME/2004/M
G18b

DEPARTMENT OF MECHANICAL ENGINEERING

Indain Institute of Technology Kapnur

JUNE, 2004

Stress Migration Failure Analysis of Aluminium Line of a Multilevel Printed Circuit Board by Boundary Element Method

A Thesis Submitted
in Partial Fulfillment of the Requirements
for the Degree of

MASTER OF TECHNOLOGY

by

Ankit Kumar Garg

to the

DEPARTMENT OF MECHANICAL ENGINEERING
INDIAN INSTITUTE OF TECHNOLOGY, KANPUR

June, 2004

27 JUL 2004 / ME
पुरुषोत्तम [illegible]
भारतीय प्रौद्योगिकी [illegible] कानपुर
प्रवाप्ति क्र० A 148431

th
ME/2004/M
G181s

A148431

POST GRADUATE OFFICE
THESIS SUBMITTED
ON 9-6-04
I.I.T., KANPUR

CERTIFICATE

It is certified that the work contained in the thesis entitled "Stress Migration **Failure Analysis of Aluminium Line of a Multilevel Printed Circuit Board by Boundary Element Method"**, by ANKIT KUMAR GARG, has been carried out under my supervision and that this work has not been submitted elsewhere for a degree.

Date:

N N Kishore 9/6
Professor N. N. Kishore
Department of Mechanical Engineering
Indian Institute of Technology Kanpur
Kanpur, 208016

Dedicated to

My Beloved Parents,

Sister Ayushi and

Fiancée Shivani

ACKNOWLEDGEMENTS

This work has made me realize that any good work is a result of efforts of many, may be directly or indirectly. I think it would not be an exaggeration if I address the present work as a team work. First and foremost, I would like to express me deep sense of respect and admiration for my thesis supervisor **Dr. N. N. Kishore.**

I thank Dr. N. N. Kishore for his invaluable guidance, numerous discussions and suggestions, constant encouragements, patient listening that he gave to my problems, and for all the knowledge that I have acquired from him. His friendly way of interacting and systematic approach made the work enjoyable. I am indebted to him for encouraging me to work on BEM, which is rather a new approach.

I would like to express my deep sense of love and gratitude for my institute, the **Indian Institute of Technology, Kanpur**. This work would not have been possible without the excellent facilities provided by the institute; the computational facilities, the digital subscription of journals, the grand central library. The beautiful work culture, high learning rate and overall atmosphere of the campus have brought significant improvements in my personality, attitude and thinking.

I express my sincere thanks to my lab-mates **Nilesh**, **Soloman**, and **Bhanu** for their support.

I express my special thanks to my class-mate **Nilesh** and **Arvind**, who help me in overcoming from the difficulties whenever I was stuck in my work.

I thank to my friends **Akshika**, **Deepak**, **Rakhi** and **Aprajita** who made my life enjoyable during my stay at IIT Kanpur. The will cherish the moments spend with them always.

I thank to my friends **Vikram** and **Shrikant** for all their affection, help and support that they extended to me during my two-year stay at IITK.

Finally, I thank the Almighty for always showing me the right path and providing me the strength and courage to move on.

Indian institute of Technology, Kanpur Ankit Kumar Garg

June 2004

ABSTRACT

Interconnectors in modern VLSI structures are getting miniaturized in cross-sectional area and in length. During processing of these structures, residual stresses are generated in the aluminium interconnections due to the thermal loading. These stresses are of very high magnitude (hundreds of MPa) and are responsible for failure of these aluminium interconnections. Some of the most significant failure mechanisms are stress migration, plastic flow and thermal grooving.

In present work, failure analysis of the above structure is being carried out with the help of Boundary Integral Method. The problem is being treated in semi coupled manner, i.e. for each time step, while cooling, a thermal analysis is performed and then the resulting temperature profile over the domain is used for stress field estimation. For transient analysis, time dependent fundamental solution scheme is used in the BEM. The Von-Mises yield criterion in plasticity is applied to examine whether the relaxation of stresses may be caused by plastic deformation. Focus has been made for maintaining the integration accuracy at sub-micron domains. The stresses-induced failure in an aluminium conductor is investigated in terms of diffusion along the surface and grain boundaries. The mechanism of thermal grooving, which initiates and grows at elevated temperature, is modeled and failure process is numerically simulated. Effect of the stress concentration near the groove tip is considered while analyzing thermal grooving.

CONTENTS

CERTIFICATE		**ii**
ACKNOWLEDGEMENTS		**iv**
ABSTRACT		**vi**
LIST OF FIGURES		**x**
CHAPTER 1	**INTRODUCTION**	**1**
1.1	Introduction	1
1.2	Literature Survey	4
1.3	Present Work and Layout of the thesis	6
CHAPTER 2	**TRANSIENT TEMPERATURE ANALYSIS AND BEM**	**8**
2.1	Problem Definition	8
2.2	BEM Introduction	10
2.3	Boundary Integral Equation and Fundamental Solution	11
2.4	Numerical Solution of the Boundary Element Equation	12
	2.4.1 Time and Space Discretization	13
	2.4.2 Shape functions for the element	15
2.5	Assembly of the different matrices for multi-layer system	16
2.6	Application of Boundary and Initial Conditions	19
2.7	Closure	21

CHAPTER 3	**THERMAL STRESS ANALYSIS**	**22**
3.1	Governing Equation	22
3.2	Boundary Integral Equation	24
3.3	Two-Dimensional Thermo-elastic Kernels	25
3.4	Numerical Implementation	26
3.5	Boundary and interface conditions	27
3.6	Modification for Nearly Singular Integral for Sub-micron Scale domain	28
	3.6.1 Regularize the nearly singular integral by singularity subtraction	29
	3.6.2 Evaluation of nearly weakly singular integral	31
3.7	Stress Relaxation	32
	3.7.1 Stresses after plastic deformation	34
3.8	Closure	36
CHAPTER 4	**THERMAL GROOVING**	**37**
4.1	Introduction	37
4.2	Estimation of thermal grooving	38
4.3	Closure	43
CHAPTER 5	**RESULTS AND DISCUSSION**	**44**
5.1	Validation of the BEM Code	44
5.2	Failure Analysis of aluminium line during Processing	45
5.3	Thermal grooving	48
CHAPTER 6	**CONCLUTION AND FUTURE SCOPE**	**65**
6.1	Conclusions	65
6.2	Scope for Future Work	66
REFERENCES		**67**
Appendix A		**70**

Appendix B 76

Appendix C 77

Appendix D 80

LIST OF FIGURES

1.1 Final multilevel structure

1.2 (a) Voids observed in aluminium line, which causes "Stress Migration" failure

(b) Photograph of the aluminum conductor in the VLSI package, which failed due to stress, induced migration

2.1 A domain V with boundary Γ

2.2 An isoperametric quadratic element

2.3 A multilayer system (Physical domain)

2.4 A multilayer system (boundary elements)

3.1 A domain V with boundary Γ

3.2 A multilayer system (physical domain)

3.3 Source point near to the line Γ of integration

3.4 Element Γ in natural coordinate system

4.1 Explanation of grooving due to diffusion along the surface and grain boundary

(a) Semi-infinite body with flat surface and grain boundary

(b) Thermal grooving due to surface diffusion

(c) Grain boundary grooving due to combination of diffusion along the surface and that along the grain boundary

4.2 Model conductor

(a) Model conductor with bamboo like structure

(b) Discritized quadrant of the conductor surface

4.3 Groove surface profile at time f and f+1

4.4 A typical node i subjected to two adjacent elements

5.1 Test Problem

5.2 Temperature variation with time at different locations

5.3 Comparison of the temperature variation with time by developed BEM code and ANSYS
5.4 Temperature profile over the domain after reaching the steady state
5.5 Temperature profile over entire domain using ANSYS at steady state
5.6 Total heat flux over the domain at steady state
5.7 Detail of Multilevel Circuit
5.8 Discritized domain for first step
5.9 Temperature variation at the middle node of the interface with time
5.10 σ_{xx} stress field distribution at the end of first step
5.11 σ_{yy} stress field distribution at the end of first step
5.12 τ_{xy} stress field distribution at the end of first step
5.13 σ_{zz} stress field distribution at the end of first step
5.14 Discritized domain for second step
5.15 Temperature variation at middle point of aluminum layer with time
5.16 σ_{zz} stress field distribution in the final structure after step 2
5.17 σ_{yy} stress field distribution in the final structure after step 2
5.18 σ_{zz} stress field distribution in the final structure after step 2
5.19 σ_{zz} stress in aluminium layer after step-2
5.20 Modelled groove profile
5.21 Groove profile, both initial and final
5.22 Groove depth with time
5.23 Normalized groove depth Vs with normalized time
5.24 Groove growth rate with time
5.25 Normalized groove growth rate Vs normalized time
5.26 Stress intensity factor Vs normalized time
5.27 T/D_s and T/D_b Vs temperature

5.28 Grain boundary (D_b) and surface (D_s) diffusion coefficients Vs temperature

D.1 Positive curvature at node i

Chapter 1

INTRODUCTION

1.1 Introduction:

Interconnectors in modern very large integrated circuits (VLSI) are getting miniaturized wherein the thickness of the conductors is reaching dimensions of less then 1μm. It, therefore, become more essential for assuring reliability to understand the failure mechanisms at submicron level, which differs greatly from those of the components of large dimensions. During fabrication, these circuits are subjected to several thermal cycles. Thus, residual stresses generate in the aluminium interconnections due to the thermal loading. These stresses are of very high magnitude (hundreds of MPa) and are responsible for failure of these aluminium interconnections. Some of the most significant failure mechanisms are plastic flow, thermal grooving and stress migration.

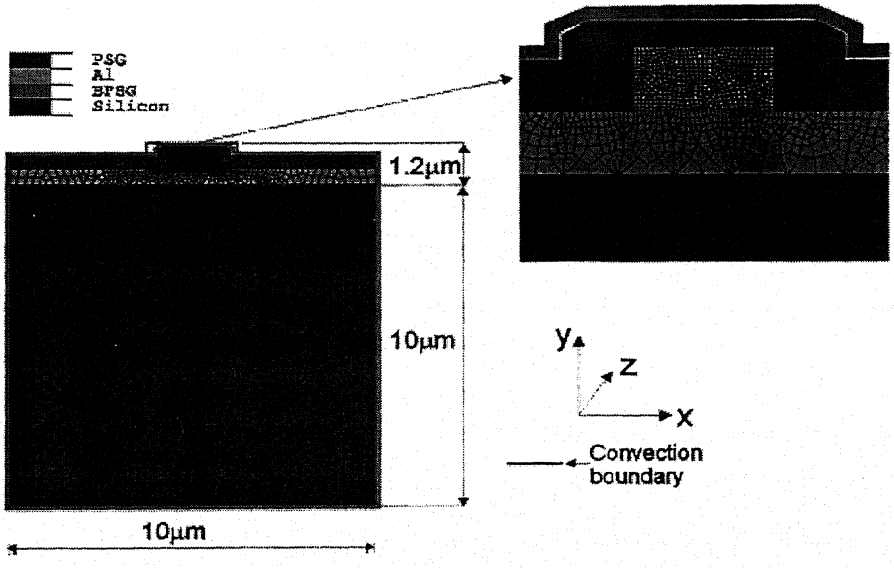

Fig 1.1: Final multilevel structure

It is well known that stress field and high temperature causes the diffusion of the atoms (or vacancies) along a grain boundary. This migration results in creep cavity and gives rise to a groove at the grain boundaries. The grooves generated prorogate even at the low temperatures due to the residual stresses in the interconnectors. This process is known as thermal grooving.

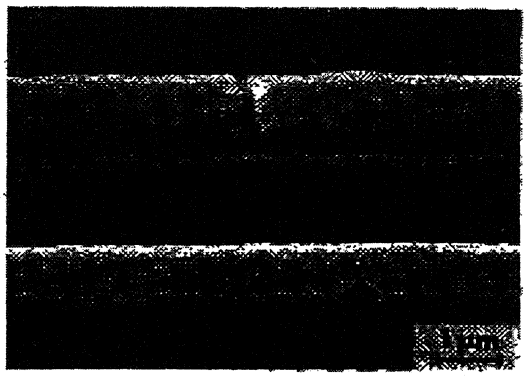

Fig 1.2a: Voids observed in Al line which causes "Stress Migration" Failure

Fig 1.2b: Photograph of the aluminium conductor in the VLSI package which failed due to stress induced migration

Stress migration is one of the principle mechanisms that cause failure of aluminium wire. This problem was first identified by Klema et al.[1] and Curry et al.[2]. This failure is caused by the nucleation and growth of the voids in the aluminium line under conditions of high stress at elevated temperatures. This process does not take into consideration the effect of current flow in the

aluminium line, where the electron wind provides a driving force to the aluminium ions. This force drives the ions to move in the conducting line and cause open-circuit-failure.

The mechanical stress which causes migration of atoms is induced during the line passivation, wherein the metal lines are covered with a glass film at high temperature and subsequently cooled down to room temperature. Since the thermal expansion coefficient of aluminium is much higher than that of the passivation films (approximately 20 times larger), the cooling process generates large thermal stresses. The existence of residual stresses is detrimental to the reliability of the aluminium interconnectors as it enhances the failure mechanism.

The boundary element method, based on the boundary integral equation formulation is well known for its accuracy and efficiency in stress analysis. In recent years, BEM has also been found to be especially accurate and efficient in the analysis of thin films. FEM studies show that very fine mesh is essential in order to accurately evaluate the interfacial stresses in thin films and coatings. For cases involving singular fields, such as interfacial cracks or free edges, even finer mesh are required, which can quickly make the domain based FEM approach costly.

Any analysis methods to assess the residual thermal stress patterns in a multilevel VLSI structure encounters two difficulties: first, the structure is subjected to several thermal cycles due to the various processing steps involved; secondly, the geometry of the structure itself changes from one fabrication step to another (as material layers are added or removed).

In the present work an advanced strategy has been applied which overcomes all previously mentioned drawbacks. With only one mesh and only one run of the program (using a so called activating-deactivating strategy) this strategy shows how to obtain the complete stress distribution during the manufacturing of the multilevel structures. The developed BEM approach can

provide not only a robust numerical tool for the analysis of multilayer systems, but also the basis for further investigations of interfacial cracks, thermal effects and contact mechanics for the multi-layer system or various thin films. For transient thermal analysis, time dependent fundamental scheme has been used. A stress induced migration failure of micron or submicron aluminium line in terms of interaction between diffusion along the surface and grain boundary takes place at high temperature levels. A numerical modeling strategy for estimation of such phenomenon has been developed which can be also be used to time to failure prediction.

1.2 Literature Survey:

Over the past three decades, due to miniaturization of electronic devices, the width of the metal interconnection lines used in integrated circuits has decreased substantially. The accompanying increase in the line aspect ratio (defined as the ratio of layer height and line width) affects the evolution of the thermal stresses, which are generated from thermal expansion mismatch between aluminium line and the surrounding materials. Numerical modelling using the finite element method has been used to predict the evolution of the stresses and the effect of line aspect ratio in metal interconnectors (Shen [3]).

Igic and Mawbay [4] presented an advanced strategy for modeling the thermal stresses induced in aluminium interconnectors during processing of multilevel structures. He performed the analysis in two steps wherein he used the residual stresses from one processing step to be used as the initial condition for the next step. Igic and Mawbay [5] presented the effect of titanium barrier layer on the residual stress in passivated multilevel aluminium metallization structure.

Mullins [6] presented a theory which describes the development of surface grooves at the grain boundaries of a heated polycrystal. These grooves develop on the surface of a hot polycrystal wherever a stationary grain boundary intersects the surface due to the diffusion of the atoms through the free surfaces and the grain boundaries. These grooves then provide early nuclei for crack initialization and propagation through grain boundaries and generate a creep like property in the aluminium interconnectors. Martinez and Nix [7] used the Mullins theory to develop finite difference technique for the diffusive growth of 2-D and axisymmetric cavities having equilibrium shapes and located on grain boundaries. The shape evaluation and growth kinematics of individual cavities as well as the time required for adjacent cavities to grow was formulated as a function of applied stress and the ratio of grain boundary to surface diffusivity. Kato et al [8] analyzed the relaxation of the residual stresses in aluminium line by plastic deformation and diffusion analytically. He extended the Mullins theory for the thermal grooving process in aluminium lines. Kitamura, Ohtani and Yamanaka [9] investigated the mechanism of grooving which initiate and grow at elevated temperature along the grain boundary and numerically simulated failure process of aluminium interconnectors. Igic and Mawbay [10] suggested an improved numerical model based on finite difference discretization for the diffusion relaxation and groove growth in the aluminium line. This model is very useful for time to failure prediction and provides better understanding of thermal grooving phenomenon.

In the last three decades, FEM based on plate and shell theories has been a successful tool for the analysis of 3-D thin structure such as layered composite structures to study their deformation and stress in the micro-scale. However, most plate and shell theories are based on various assumptions about the geometry, loading and deformation of the structure, and therefore the accuracy and reliability of the FEM for the thin structures in the micro or nanoscales are

in doubt. The BEM based on the elasticity theory and boundary integral equation formulation (Banerjee [11]) is in general more accurate in stress analysis of thin structures.

Pina and Fernandes [12] presented a boundary element formulation for three dimensional time-dependent heat conduction problems in homogeneous isotropic bodies using a time marching scheme which does not require the discretization of domain. Pasquetti, Curso and Wrobel [13] proposed a time dependent fundamental scheme to solve transient heat transfer problem. This scheme was found very efficient and easy to apply and did not need any domain integral. Luo, Liu and Berger [14] developed a model for the application of the boundary integral method in the (2-D) thin structures with the thickness to length ration in the micron or nanoscales. He presented an efficient analytical method to deal with the nearly singular integrals. In addition, he proposed a new nonlinear coordinate transformation for nearly singular integrals to further increase the numerical accuracies. Luo, Liu and Berger [15] advanced his boundary integral model for 2-D thin structure to the analysis of interfacial stresses for multi-coating systems. He also supplied a basis for the analysis of interfacial cracks, thermal effects and contact mechanics using boundary integral method.

Chen and Liu [16] developed an advanced boundary integral method for analyzing thin layered structures under the steady state thermal loading and also compared the thermal BEM with commercial FEM software for the multi-layered structures of nanoscale dimensions.

1.3 Present Work and Layout of the Thesis:

The objective of the present work is to determine the stress field of an aluminium layer in multilayer VLSI structure subjected to cyclic thermal

loading during and after processing. First the temperature profiles due to various fabrication steps have been solved. During thermal loading structure is subjected to natural convection boundary conditions. The resulting temperature profile has been used to get the residual stresses in the structure. Thermal grooving process which occurs due to the residual stresses in aluminium layer has been analyzed. Focus has been made for accurate evaluation of domain integrals for sub-micro scale domain. The boundary integral method has been made use of for accurately performing the above task.

The thesis has six chapters and each of them is self contained unit.

In Chapter 2, the 2-D transient heat conduction formulation is described using time dependent fundamental scheme. This chapter also includes a discussion on the treatment of various types of initial conditions and an efficient convolution-type time-marching scheme.

Chapter 3 deals with the thermal stress analysis for two dimensional problems. Thermal effects over the solution domain are treated to calculate stress fields. Effect of the multiple domains and special consideration for evaluating integrals at the sub-micron scale are explained. A simplified model for the stress relaxation due to plastic deformation is also explained.

In Chapter 4, the stress induced failure in aluminium interconnectors is investigated in terms of diffusion along the surface and along the grain boundary. A numerical model dealing with thermal grooving process has also been described.

In Chapter 5, the results have been presented for stress analysis during processing and thermal grooving phenomenon after the processing.

Finally, in Chapter 6, the work is summarized and the relevant conclusions and the scope for the future work are presented.

Chapter 2

TRANSIENT TEMPERATURE ANALYSIS AND BEM

This Chapter describes boundary element formulation for transient heat conduction using time dependent fundamental solution. Numerical techniques are then employed to solve the integral equations in discrete form through time marching procedure. Space and time discretization algorithm are discussed in detail for two dimensional problems and expressions resulting from the analytical integration of the fundamental solutions with respect to time are included. The next section describes how linear boundary conditions are implemented.

The BEM formulation is given in brief and all salient points of the method relevant to present problem have been brought out clearly. This temperature field will be used to evaluate residual stresses and thermal grooving in the next chapters.

2.1 Problem Definitions:

The governing differential equation for transient heat conduction can be written as [15]

$$\nabla^2 T + b = \frac{1}{k}\frac{\partial T}{\partial t} \tag{2.1}$$

where T is temperature, t is time, k is thermal diffusivity ($k = \lambda/\rho c$), λ is the thermal conductivity, ρ is density, c is specific heat, and the term b represents the internal heat generation.

The most common boundary conditions in heat transfer problem are of the following types:

- Dirichlet condition (prescribed temperature):

$$T = T \qquad \text{on } \Gamma_1 \qquad (2.2)$$

- Neumann condition (prescribed flux):

$$q = \frac{\partial T}{\partial n} = q \qquad \text{on } \Gamma_2 \qquad (2.3)$$

- Fourier condition (convection):

$$p(T) = -h(T - T_\alpha) + \phi \qquad \text{on } \Gamma_3 \qquad (2.4)$$

in which h is the heat transfer coefficient, T_α is the ambient temperature and Φ is a known value. The adopted convection implies that q is positive if the surfaces flux $p = \lambda q$ is inwards the region. Moreover, α and β may vary in space and time.

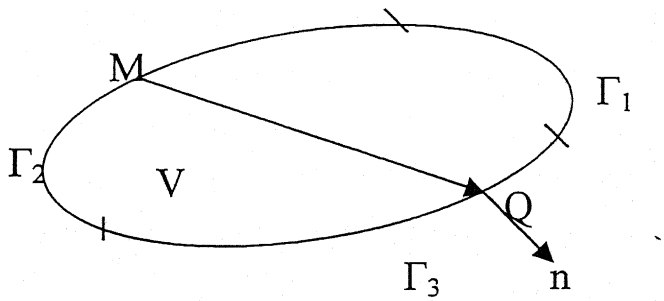

Fig 2.1: A domain V with boundary Γ

The present problem is being solved in two steps. In first step BPSG layer is put over the silicon layer at passivation temperature and cooled down to room temperature. While in the Step-2 aluminium layer passivated with PSG layer is deposited over the BPSG layer. Thus, for the first step, the initial temperature profile is constant passivation temperature, while in the next step the temperature profile calculated from first step is being used as the initial condition.

2.2 BEM Introduction:

The BEM is a numerical technique based on integral equation formulation of the continuum mechanics problems. There are two types of integral equation formulation. One contains, as basic unknowns quantities with a clear physical meaning. This type is called the direct formulation. In the second type, known as indirect formulation, the basic unknown quantities have no physical meaning. The physical variables are obtained from these quantities. In present work, numerical approach used is based on direct formulation [15].

There are some general characteristics of the BEM which lead to advantages for the analysis of static and dynamic continuum mechanics problems. First of all, as the equations are formulated in terms of variables on the boundary, only the boundary has to be discretized as opposed to domain techniques, such as Finite Element Method (FEM) and the Finite Difference Method (FDM). As a consequence, the resulting number of equations is smaller in the BEM. This leads to less data preparation and less requirement of computer time and storage. Another consequence is that the mesh generation process is simpler than in domain type methods. This advantage is important for the situation where the geometry changes throughout the solution process, as in crack propagation study, processing of multilayer or multi-coating structures, etc. A second characteristic of the BEM is that it produces accurate solutions on the boundary and in particular at any selected internal point. This feature makes the method very appropriate for problem where high accuracy is required.

Among the disadvantages of BEM, first is the mathematical complexity in BE formulation is more (evaluation of Green function). The solution matrix resulting from the BE formulation is unsymmetric and fully populated with nonzero coefficients. This means that the entire solution matrix is needed to be saved in the computer memory. Second disadvantage is its difficulty in dealing

with non-linear material properties. In such cases the integral equations include domain integrals and the advantages of a boundary formulation vanish if there are many non-linear material zones.

2.3 Boundary Integral Equation and Fundamental Solution:

The governing heat conduction equations (2.1) to (2.4) can be recast as an integral equation over space and time [13]. Divergence theorem is used to convert the governing differential equation into a boundary integral equation as follows:

$$c_M T_{M,t_F} + \int_{t_0}^{t_F} \int_{\Gamma} kTq^* \partial\Gamma dt = \int_{t_0}^{t_F} \int_{\Gamma} kqT^* \partial\Gamma dt + \int_{t_0}^{t_F} \int_{V} kbT^* \partial\Omega dt + \int_{V} T_0 T^* \partial\Omega \tag{2.5}$$

where T_{M,t_F} is temperature at point M at time t_F, c_M is a coefficient depending on the geometry of Γ at point M, k is thermal diffusivity, T temperature profile at the boundary Γ, T_0 is initial temperature profile over the domain, b is body force, $q = \frac{\partial T}{\partial n}, q^* = \frac{\partial T^*}{\partial n}$, and $\vec{n}$ is the unit outward normal vector.

The fundamental solution T^* describes the temperature field due to a unit heat source applied at pint M at time t_0. Many researches have given different fundamental solutions of different accuracies (Chandra, Chan and Lim [18], Koizumi, Utamura and Kotani [19]). In the present work the fundamental solution given by Wrobel and Brebbia [11] is used, which is given by,

$$T^*(r,\tau) = \frac{1}{(4\Pi k\tau)^{s/2}} \exp^{(-\frac{r^2}{4k\tau})} \tag{2.6}$$

$$q^*(r,\tau) = \frac{2d}{(4k\tau)^{(s+2)}\Pi^{s/2}} \exp^{(-\frac{r^2}{4k\tau})} \tag{2.7}$$

with $d = -\vec{n}.\vec{r}$, $\vec{r}$ being the position vector connecting source and field points, $\tau = t_F - t$ and s is the number of spatial dimension of the problem.

This formulation can also be applied to non-linear problems in which the thermal conductivity λ is a function of temperature. In this case, it is convenient to employ the Kirchhoff Transformation,

$$\psi = \int_{T_r}^{T} \lambda(T')dT' \tag{2.8}$$

where T_r is the reference temperature. For steady state problems, the above transformation is sufficient to linearize the governing equation. For transient problems, the integration by parts of the equation (2.1) weighted by T^* gives rise to additional domain integrals involving the derivatives of k. Assuming, that the space and time derivatives of k are small quantities and can be neglected, then,

$$\vec{\nabla} k \simeq \vec{0}$$

$$\frac{\partial k}{\partial t} \simeq 0 \tag{2.9}$$

An integral equation similar to (2.2) is obtained for the non-linear problem [17]

$$c_M \psi_{M,t_F} + \int_0^{t_F} \int_\Gamma k\psi q^* \partial\Gamma dt = \int_0^{t_F} \int_\Gamma kpT^* \partial\Gamma dt + \int_0^{t_F} \int_V kgT^* \partial\Omega dt + \int_V \psi_0 T^* \partial\Omega \tag{2.10}$$

2.4 Numerical Solution of the Boundary Integral Equation:

The numerical solution of the boundary integral equation (2.5) and (2.10) requires space and time discretization. Two different time-marching schemes can be used in the solution:

1. For each time step, to calculate temperature at the resolution time t_F, the temperature at the previous the time level t_{F-1} is taken as initial

temperature. This approach minimizes the time integrations but requires the evaluation of the domain integral associated with the temperature field T_{F-1} at each time step;

2. For each time step, the solution is restarted from the initial time t_0; in this way, the domain integral associated to the initial conditions can be avoided for the majority of practical situations.

The second approach was adopted in this work. Recently, truncation algorithms were developed [13] to improve the computer efficiency of such an approach. One such algorithm, named 'steady temporal domain', is herein presented in detail.

2.4.1 Time and space discretization:

Equation (2.5) represents two domain integrals due to initial conditions and internal source. For simplicity, if there is no internal heat generation and that the initial temperature is constant, then it is possible to rewrite the problem into an equivalent one with zero initial value for temperature difference ($T - T_0$). For the non-linear case, it is sufficient to take T_0 as reference temperature T_r in the Kirchhoff transformation.

With the above simplification, Eq. (2.5) can be written for a point M in the portion of Γ as

$$\frac{1}{2}T_{M,t_F} + \int_0^{t_F}\int_\Gamma kTq^*\partial\Gamma dt = \int_0^{t_F}\int_\Gamma kqT^*\partial\Gamma dt \qquad (2.11)$$

Dividing the boundary Γ into N boundary elements and the time span ($t_F - t_0$) into F time steps, the following discretized equation is obtained

$$\frac{1}{2}T_{M,t_F} + \sum_{f=1}^{F}\sum_{j=1}^{N}\int_{t_{f-1}}^{t_f}\int_{\Gamma_j} k\psi q^*\partial\Gamma dt = \sum_{f=1}^{F}\sum_{j=1}^{N}\int_{t_{f-1}}^{t_f}\int_{\Gamma_j} kqT^*\partial\Gamma dt \qquad (2.12)$$

where $T_{i,F}$ being the temperature at node i at time t_F.

Assuming that the variables are linear in each time step, the temperature variation on element j between time interval f-1 and f is given by

$$T = \frac{T_{j,f-1}(t_f - t) + T_{j,f}(t - t_{f-1})}{\Delta t_f} \tag{2.13}$$

with $\Delta t_f = t_f - t_{f-1}$. A similar expression can be written for q. Writing

$$H1_{i,j,F,f} = \frac{1}{\Delta t_{f-1}} \int_{f-1}^{f} \int_{\Gamma_j} k(t_f - t) T^* \partial\Gamma dt \tag{2.14}$$

$$\hat{H}2_{i,j,F,f} = \frac{1}{\Delta t_{f-1}} \int_{f-1}^{f} \int_{\Gamma_j} k(t - t_{f-1}) T^* \partial\Gamma dt \tag{2.15}$$

$$G1_{i,j,F,f} = \frac{1}{\Delta t_{f-1}} \int_{f-1}^{f} \int_{\Gamma_j} k(t_f - t) T^* \partial\Gamma dt \tag{2.16}$$

$$G2_{i,j,F,f} = \frac{1}{\Delta t_{f-1}} \int_{f-1}^{f} \int_{\Gamma_j} k(t - t_{f-1}) T^* \partial\Gamma dt \tag{2.17}$$

$$H2_{i,j,F,f} = \hat{H}2_{i,j,F,f} + \frac{1}{2}\delta_{i,j}\delta_{F,f} \tag{2.18}$$

in which δ is the Kronecker delta, the relations Eq. (2.12) can be written as:

$$\sum_{f=1}^{F}\sum_{j=1}^{N}(H1_{i,j,F,f}T_{j,f-1} + H2_{i,j,F,f}T_{j,f}) = \sum_{f=1}^{F}\sum_{j=1}^{N}(G1_{i,j,F,f}q_{j,f-1} + G2_{i,j,F,f}q_{j,f}) \tag{2.19}$$

Writing the above equation at all boundary nodes i ($1 \le i \le N$) using a collocation technique, the following system of equations is obtained

$$\sum_{f=1}^{F}(H1_{F,f}T_{f-1} + H2_{F,f}T_f) = \sum_{f=1}^{F}(G1_{F,f}Q_{f-1} + G2_{F,f}Q_f) \tag{2.20}$$

The temperature and flux at each node are known for all time levels previous to t_F, so that the above equation can be rewritten in the form

$$H2_{F,f}T_f = G2_{F,F}Q_F + S_F \tag{2.21}$$

with

$$S_F = \sum_{f=1}^{F}(H1_{F,f}T_{f-1} + H2_{F,f}T_f) - H1_{F,F}T_{F-1} + \sum_{f=1}^{F-1}(G1_{F,f}Q_{f-1} + G2_{F,f}Q_f) + G1_{F,F}Q_{F-1} \tag{2.22}$$

The details of evaluation of H1, H2, G1 and G2 can be found in Appendix 'A'.

2.4.2 Shape functions for the element:

The boundary of the solution domain is divided into a number of connected elements. The variation of geometry and variables over element may be constant, linear, quadratic, cubic or higher order and the variation may be different for both geometry and the variables. Increasing the order of variation of an element produces accurate solutions, but the penalty of higher CPU must be paid. These variations of geometry and variables over an element are prescribed by defining the "Shape functions". The geometry of a 3-noded quadratic element can be described by the coordinates of its three nodes and the shape function as follows:

$$\begin{aligned} x(\eta) &= \sum_{c=1}^{3} N_c(\eta)x_c = N_1(\eta)x_1 + N_2(\eta)x_2 + N_3(\eta)x_3 \\ y(\eta) &= \sum_{c=1}^{3} N_c(\eta)y_c = N_1(\eta)y_1 + N_2(\eta)y_2 + N_3(\eta)y_3 \end{aligned} \tag{2.23}$$

where the shape function can be defined as

$$\begin{aligned} N_1 &= \frac{-\eta}{2}(1-\eta) \\ N_2 &= (1+\eta)(1-\eta) \\ N_3 &= \frac{\eta}{2}(1+\eta) \end{aligned} \tag{2.24}$$

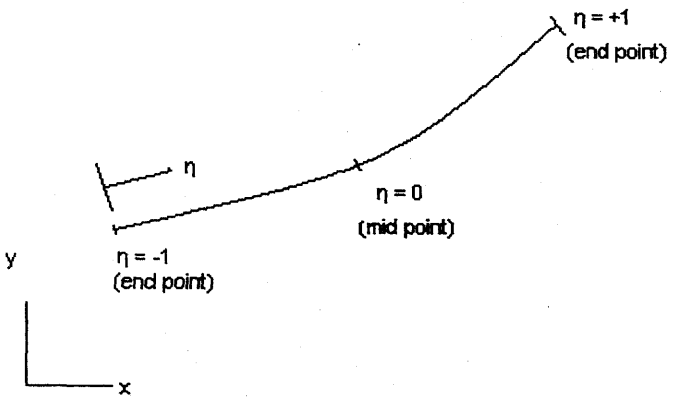

Fig 2.2: An isoperametric quadratic element

Isoperaimetric elements are being used in the present analysis. Therefore, the shape functions will be same to define the solution variables, as follows:

$$T(\eta)=\sum_{c=1}^{3}N_c(\eta)T_c=N_1(\eta)T_1+N_2(\eta)T_2+N_3(\eta)T_3$$
$$\frac{\partial T(\eta)}{\partial n}=\sum_{c=1}^{3}N_c(\eta)\left(\frac{\partial T}{\partial n}\right)_c=N_1(\eta)\left(\frac{\partial T}{\partial n}\right)_1+N_2(\eta)\left(\frac{\partial T}{\partial n}\right)_2+N_3(\eta)\left(\frac{\partial T}{\partial n}\right)_3 \tag{2.25}$$

2.5 *Assembly of the Different Matrices for Multi-layer System:*

Fig (2.3) and (2.4) show physical and mathematical schematic diagrams of a multi-layer system, respectively. The boundary and interface conditions for each layer can be written as follows:

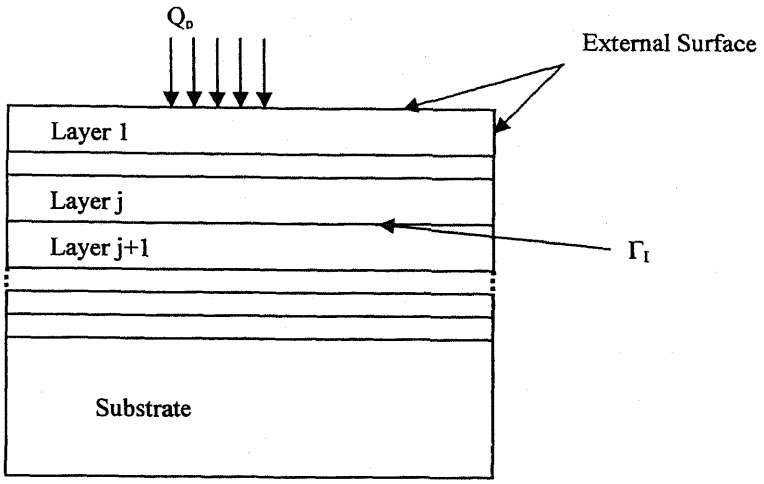

Fig. 2.3: A multilayer system (Physical domain)

- On the boundary (external surface) of the multi-layer system, the heat flux or temperature should be prescribed:

$$Q = Q_P \tag{2.26a}$$

or,

$$T = T_P \tag{2.26b}$$

where Q is heat flux on the surface, Q_p is applied heat flux, T is temperature on the boundary and T_p is prescribed temperature.

- On every interface Γ_I between layers j and j+1 heat flux and temperature satisfy the continuity condition:

$$\begin{aligned} Q_I &= Q_I^{\,j} = -Q_I^{\,j+1} \\ T_I &= T_I^{\,j} = T_I^{\,j+1} \end{aligned} \tag{2.27}$$

where the subscript I indicates I^{th} interface.

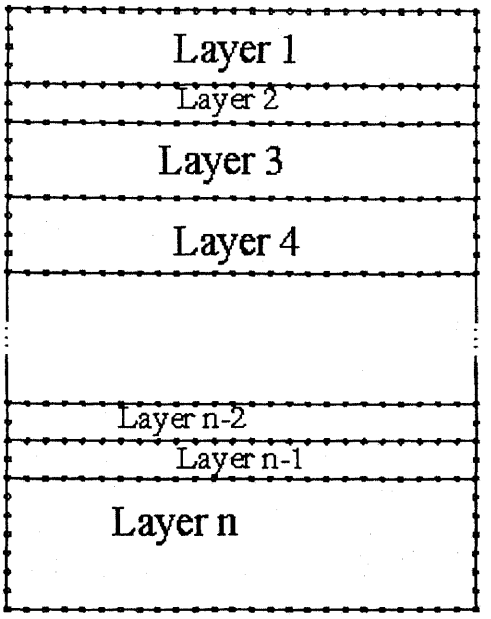

Fig. 2.4 A multilayer system (boundary elements)

It is important to note that only the perfectly bonded part satisfies the above equilibrium conditions. The non-perfectly bonded part, say, an interface crack, will be considered as an additional boundary of each layer and the heat flux and temperature values associated with them will not be coupled together in the final equation.

The conditions at the interface, I between layers j and j+1 as given in Eq. 2.27 can be implemented in boundary element equations as follows.

For the jth layer, the temperature and heat flux are related by,

$$\begin{bmatrix} H^j & H_I^j \end{bmatrix} \begin{bmatrix} T^j \\ T_I^j \end{bmatrix} = \begin{bmatrix} G^j & G_I^j \end{bmatrix} \begin{bmatrix} Q^j \\ Q_I^j \end{bmatrix} \tag{2.28}$$

where T_I^j and Q_I^j are the interface temperatures and heat flux of layer j on the interface Γ_I, T^j and Q^j the temperature and heat flux on the remaining surfaces.

Similarly, for the layer j+1, the relationship can be written as,

$$\begin{bmatrix} H^{j+1} & H_I^{j+1} \end{bmatrix} \begin{bmatrix} T^{j+1} \\ T_I^{j+1} \end{bmatrix} = \begin{bmatrix} G^{j+1} & G_I^{j+1} \end{bmatrix} \begin{bmatrix} Q^{j+1} \\ Q_I^{j+1} \end{bmatrix} \tag{2.29}$$

where T_I^{j+1} and Q_I^{j+1} are the interface temperatures and heat flux of layer j+1 on the interface Γ_I, T^{j+1} and Q^{j+1} the temperature and heat flux on the remaining surfaces.

According to the equilibrium condition (2.27) at an interface, Eqs. (2.28) and (2.29) can be rewritten as [6]:

$$\begin{bmatrix} H^j & H_I^j & -G_I^j \end{bmatrix} \begin{bmatrix} T^j \\ T_I^j \\ Q_I^j \end{bmatrix} = \begin{bmatrix} G^j \end{bmatrix} \begin{bmatrix} Q^j \end{bmatrix}$$

and

$$\begin{bmatrix} H^{j+1} & H_I^{j+1} & G_I^{j+1} \end{bmatrix} \begin{bmatrix} T^{j+1} \\ T_I^{j+1} \\ Q_I^{j+1} \end{bmatrix} = \begin{bmatrix} G^{j+1} \end{bmatrix} \begin{bmatrix} Q^{j+1} \end{bmatrix}$$

respectively. Thus, coupling of the above two equations yields the equation,

$$\begin{bmatrix} H^j & H_I^j & -G_I^j & 0 \\ 0 & H_I^{j+1} & G_I^{j+1} & H^{j+1} \end{bmatrix} \begin{bmatrix} T^j \\ T_I^j \\ Q_I^j \\ T^{j+1} \end{bmatrix} = \begin{bmatrix} G^j & 0 \\ 0 & G^{j+1} \end{bmatrix} \begin{bmatrix} Q^j \\ Q^{j+1} \end{bmatrix} \tag{2.30}$$

Similar equations can be derived for other layers and the substrate. The system needs to be reordered to make the matrix equation in banded form.

2.6 *Application of Boundary and Initial Conditions:*

With the boundary conditions (2.2) to (2.4), the equation relative to the boundary points (2.19) can be decomposed as follows:

$$\sum_{j(1)} H2_{i,j,F,F}\overline{T}_{j,F} + \sum_{j(2)} H2_{i,j,F,F}T_{j,F} + \sum_{j(3)}\left(H2_{i,j,F,F} - G2_{i,j,F,F}\alpha_j\right)T_{j,F} =$$
$$\sum_{j(1)} G2_{i,j,F,F}q_{j,F} + \sum_{j(2)} G2_{i,j,F,F}\overline{q}_{j,F} + \sum_{j(3)} G2_{i,j,F,F}\beta_{j,F} + S_{i,F} \tag{2.31}$$

where j(k) means element j is in part Γ_k of the boundary. Writing the above equation for all boundary points produces the system

$$H2^*_{F,F}T_F = G2_{F,F}Q_F + S^*_F \tag{2.32}$$

For linear time variation, if j $\in \Gamma_1$ or Γ_2,

$$H2^*_{i,j,F,F} = H2_{i,j,F,F}$$

$$S^*_{i,F} = S_{i,F}$$

and if j $\in \Gamma_3$,

$$H2^*_{i,j,F,F} = H2_{i,j,F,F} - G2_{i,j,F,F}\alpha_j$$

$$S^*_{i,F} = S_{i,F} + \sum G2_{i,j,F,F}\beta_j$$

Consider that the initial temperature field T_0 satisfies the equation

$$\nabla^2 T_0 + b_0 = 0 \tag{2.33}$$

in which b_0 is the value of b at time t_0. Using the above equation in Eq. (2.1), it can be obtained

$$\nabla^2(T - T_0) + b - b_0 = \frac{1}{k}\frac{\partial T}{\partial t} = \frac{1}{k}\frac{\partial}{\partial t}(T - T_0) \tag{2.34}$$

with the initial condition $T - T_0 = 0$ at time t_0.

The boundary integral equation equivalent to Eq. (2.34) is

$$c_M\left(T_{M,t_F} - T_{M,0}\right) + \int_{t_0}^{t_F}\int_\Gamma k\left(T - T_0\right)q^* d\Gamma dt =$$
$$\int_{t_0}^{t_F}\int_\Gamma k\left(q - q_0\right)T^* d\Gamma dt + \int_{t_0}^{t_F}\int_\Omega k\left(b - b_0\right)T^* d\Omega dt \tag{2.35}$$

The temperature profile over the entire domain can be calculated after knowing variation of temperature over entire boundary using Eq. (2.5). However,

this does not require time dependent fundamental solution. A simpler solution may be used as given in Appendix 'B'.

2.7 Closure:

In this Chapter, the basic theory for the transient temperature analysis using time dependent fundamental scheme has been presented. Application of the boundary and initial conditions has also been given. The modification in the modeling for the multilayer systems has also been described.

Chapter 3

THERMAL STRESS ANALYSIS

In this Chapter the temperature field as determined in Chapter 2 will be used to investigate a thermo-elastic stresses and failure mechanisms. This formulation treats the thermal effects as body forces over the solution domain. The body force term is a domain integral which would normally require the discretization of the domain into cells. Therefore, these domain integral terms are transformed into boundary integrals, preserving the important advantage of the BE technique.

Special emphasis is needed on the accurate evaluation of boundary integrals for sub-micro scale domain. If the materials yield at any point, then the stress relaxation by plastic deformation is also taken into consideration.

3.1 Governing Equation:

For the case of a material being elastic, homogeneous and isotropic continuum, the equilibrium of forces and conservation of energy together with the constitutive laws yield the following system of governing equations within the linear theory of thermo-elasticity [17],

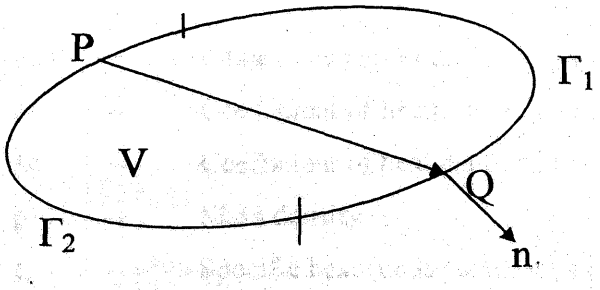

Fig 3.1: A domain V with boundary Γ

$$\mu u_{i,kk} + (\chi + \mu) u_{k,ki} + X_i = \rho d^2 u / dt^2 + \gamma \phi_{,i} \tag{3.1}$$

$$\phi_{,kk} - \frac{1}{k}\dot{\phi} - \varepsilon \dot{u}_{k,k} = -\frac{Q}{\kappa_o} \tag{3.2}$$

in which $u_i(x,t)$ and $\Phi_i(x,t)$ are the displacement and temperature fields, respectively, and χ, μ are material properties as given below. For the thermo-elastic analysis Φ is the deviation of the current temperature T from the value T_0 corresponding to the undeformed state. The symbols $X_i(x,t)$ and $Q(x,t)$ denote the intensities of the body force vector and the heat sources. The relationships between various material parameters employed in Eq. (3.1) and (3.2) are:

Table 3.1: Relationships of material properties

Parameter	χ	γ	ε	$1/\kappa$
3-d problems Plain strain	λ	γ_o	ε_o	$1/\kappa_o$
Plane stress	$2\mu\frac{\upsilon}{1-\upsilon}$	$2\mu\alpha\frac{1+\upsilon}{1-\upsilon}$	$\varepsilon_o\frac{1-2\upsilon}{1-\upsilon}$	$\frac{1}{\kappa_o}+\frac{1+\upsilon}{1-\upsilon}\varepsilon_o\alpha$

with

$$\gamma_o = (2\mu + 3\lambda)\alpha, \quad \varepsilon_o = \frac{\gamma_o T_o}{\lambda_o}, \quad \kappa_o = \frac{\lambda_o}{\rho c_\varepsilon}$$

μ, λ	--	Lame constant (under isotropic condition)
α	--	Coefficient of linear thermal expansion
λo	--	Coefficient of heat conduction
ρ	--	Mass density
c_ε	--	Specific heat (under constant strain)
κ	--	Thermal diffusivity
υ	--	Poission's ratio

The tensor of elastic constants for a homogeneous and isotropic continuum is given by

$$c_{ijkl} = \chi\delta_{ij}\delta_{kl} + \mu(\delta_{ik}\delta_{jl} + \delta_{il}\delta_{jk}) \tag{3.3}$$

The constitutive law that includes deformations and temperature (known as the Duhamel-Neumann relation) is given as,

$$\sigma_{ij} = 2\mu_{ij} + (\chi\varepsilon_{kk} - \gamma\phi)\delta_{ij} \tag{3.4}$$

This can be rewritten as

$$\sigma_{ij} = c_{ijkl}\varepsilon_{kl} - \gamma\phi\delta_{ij} \tag{3.5}$$

In general, the boundary conditions for the thermal stress analysis can be given as:

- Domain should have prescribed tractions at some part of the boundary, i.e.

$$T_n = \overline{T}_n \qquad \text{on } \Gamma_1 \tag{3.6}$$

- Remaining part of the boundary should be constrained, i.e.

$$u_n = \overline{u}_n \qquad \text{on } \Gamma_2 \tag{3.7}$$

3.2 Boundary Integral Equation:

The above governing equations can be recast as a three-dimensional boundary integral form having body force volume integral (considering no heat source) as [16]:

$$u_i(p) + \int_S T_{ij}(p,Q)u_j(Q)dS(Q) = \int_S U_{ij}(p,Q)t_j(Q)dS(Q) + \int_V U_{ij}(p,q)X_j(q)dV(q) \tag{3.8}$$

where S is the surface and V is the volume. $T_{ij}(p,Q)$ and $U_{ij}(p,Q)$ are called traction and displacement kernels and can be given for two-dimensional problems as:

$$U_{ij}(p,Q)=\frac{1}{8\pi\mu(1-\upsilon)}\left\{(3-4\upsilon)\ln\left[\frac{1}{r(p,Q)}\right]\delta_{ij}+\frac{\partial r(p,Q)}{\partial x_i}\frac{\partial r(p,Q)}{\partial x_j}\right\} \tag{3.9}$$

$$T_{ij}(p,Q)=\frac{-1}{4\pi(1-\upsilon)r(p,Q)}\left(\frac{\partial r(p,Q)}{\partial n}\right)\left\{(1-2\upsilon)\delta_{ij}+2\frac{\partial r(p,Q)}{\partial x_i}\frac{\partial r(p,Q)}{\partial x_j}\right\} \tag{3.10}$$

$$+\frac{1-2\upsilon}{4\pi(1-\upsilon)r(p,Q)}\left[\frac{\partial r(p,Q)}{\partial x_j}n_i-\frac{\partial r(p,Q)}{\partial x_i}n_j\right]$$

The body force vector, $X_j(q)$ can be expressed as the gradient of a potential function, $\Phi(q)$, as:

$$X_j(q)=\frac{-\alpha E}{1-2\upsilon}\frac{\partial\phi(q)}{\partial x_j} \tag{3.11}$$

Eq. (3.8) is valid for both 2-D plane strain and 3-D generalized plane strain problems. The effective coefficient of thermal expansion for two-dimensional problems is therefore given by

$$\alpha^* = \alpha \qquad \text{(Plane strain)}$$

$$\alpha^* = \alpha\frac{1+\upsilon}{1+2\upsilon} \qquad \text{(Plane stress)} \tag{3.12}$$

3.3 Two-Dimensional Thermo-Elastic Kernels:

From the boundary integral equation (3.8), using divergence theorem the body force term can be modelled in the following form [17]:

$$B_i=\int_\Gamma M_i(p,Q)\phi(Q)d\Gamma(Q)+\int_\Gamma N_i(p,Q)\frac{\partial\phi(Q)}{\partial n}d\Gamma(Q) \tag{3.13}$$

and, the two-dimensional thermo-elastic kernels can be written as follows:

$$M_i=\frac{\alpha(1+\upsilon)}{8\pi(1-\upsilon)}\frac{\partial}{\partial n}\left\{\frac{\partial}{\partial x_i}\left[r^2(p,Q)\ln r(p,Q)\right]\right\} \tag{3.14}$$

$$N_i=\frac{-\alpha(1+\upsilon)}{8\pi(1-\upsilon)}\frac{\partial}{\partial x_i}\left[r^2(p,Q)\ln r(p,Q)\right] \tag{3.15}$$

These kernels can be further expanded to

$$M_i = \frac{-\alpha(1+\upsilon)}{8\pi(1-\upsilon)}\left\{\left[2\ln r(p,Q)-1\right]n_i + 2\frac{\partial r(p,Q)}{\partial x_i}\frac{\partial r(p,Q)}{\partial n}\right\} \tag{3.16}$$

$$N_i = \frac{\alpha(1+\upsilon)}{8\pi(1-\upsilon)} r(p,Q)\frac{\partial r(p,Q)}{\partial x_i}\left[2\ln r(p,Q)-1\right] \tag{3.17}$$

3.4 Numerical Implementation:

The evaluation of the kernels is achieved by dividing the surface (boundary) into elements and performing the numerical integration over each element. Therefore, the discretized form of the BIE can be written as:

$$C_{ij}(P)u_i(P) + \sum_{m=1}^{M}\sum_{c=1}^{L} u_j(Q)\int_{-1}^{1} T_{ij}(P,Q)N_c(\xi)J(\xi)d\xi = \sum_{m=1}^{M}\sum_{c=1}^{L} t_j(Q)\int_{-1}^{1} U_{ij}(P,Q)N_c(\xi)J(\xi)d\xi$$
$$+\sum_{m=1}^{M}\sum_{c=1}^{L}\phi(Q)\int_{-1}^{1} M_i(P,Q)N_c(\xi)J(\xi)d\xi + \sum_{m=1}^{M}\sum_{c=1}^{L}\frac{\partial\phi(Q)}{\partial n}\int_{-1}^{1} N_i(P,Q)N_c(\xi)J(\xi)d\xi \tag{3.18}$$

where M is the total number of elements and L is the number of nodes per element (eight for three-dimensional quadratic elements). Taking each node in turn as the load point P and performing the integrations, a set of linear algebraic equations emerges as follows:

$$[A][u] = [B][t] + [F][\phi] + [G]\left[\frac{\partial\phi}{\partial n}\right] \tag{3.19}$$

where the matrices A and B contains the integrals of kernels U_{ij} and T_{ij}, respectively, while the matrices F and G contain the integrals of the thermo-elastic kernels, M_i and N_i, respectively.

As mentioned earlier, the temperature and temperature gradient calculated from transient analysis must be substituted in Eq. (3.28). No further manipulations are necessary to form the solution matrix, because the thermo-

elastic contributions are simply added to the right hand side of the solution matrix, as follows:

$$[A^*][x]=[B^*][y]+[f]+[g] \tag{3.20}$$

where [x] contains all the unknown functions (whether displacements or tractions), and [y] contains all prescribed values (whether displacements or tractions).

3.5 Boundary and Interface Conditions:

Assembly of the [A], [B], [F] and [G] for the multilayer can be done in the similar way as descried in the section 2.5. The boundary and the interface conditions now can be given as:

- On the boundary (external surface) of the multi-layer system, the traction must be given, such as:

$$t_n = \overline{t}_n, t_t = \overline{t}_t \tag{3.21}$$

where, t_n and t_t are the normal and tangential components of the traction, $\overline{t}_n$ and $\overline{t}_t$ the applied loads in the normal and directions, respectively. In addition, the multi-layer system should be constrained (with specified displacement) at some other location of boundary.

- On every interface Γ_I between layers j and j+1 normal and tangential traction and displacements from both sides of the interface satisfy:

$$\begin{aligned} t_{In} &= t_{In}{}^{j} = -t_{In}{}^{j+1}, t_{It} = t_{It}{}^{j} = -t_{It}{}^{j+1} \\ u_{In} &= u_{In}{}^{j} = u_{In}{}^{j+1}, u_{It} = u_{It}{}^{j} = u_{It}{}^{j+1} \end{aligned} \tag{3.22}$$

where the subscript In indicates normal traction component at interface (I), and subscript It indicates tangential traction component at interface (I).

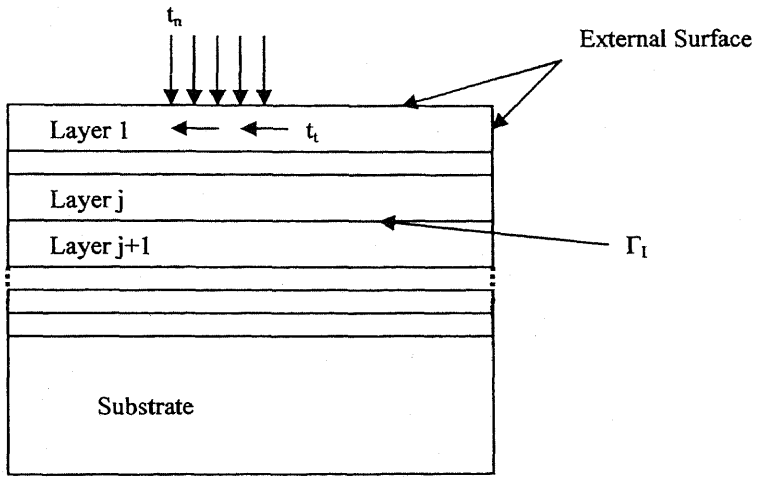

Fig. 3.2: A multilayer system (physical domain)

An advantage for the BEM as applied to multi-domain problems is that both traction equilibrium and displacement compatibility conditions between layers are explicitly satisfied, as compared to FEM, in which only the displacement compatibility condition is explicitly satisfied [13].

3.6 Modification for Nearly Singular Integral for Sub-micro scale domains:

The difficulty in applying the BEM for thin-structure and crack problems is the evaluation of nearly singular integrals. The integrals in BEM, which determine the influences matrices, contain singular kernels of the order O(1/r) and O(ln r) in 2-D elasticity case, where r is the distance between the source point and the integration point on the boundary element. When the source point is very close to, but not on the element ($0 < e << 1$, where e being the distance between source point and element of integration), although the kernels are regular in

mathematical sense, the values of the kernels change steeply in the neighborhood of the source point [12]. The standard Gaussian-quadrature is no longer practical in this case since a large number of integration points are needed in order to achieve a required accuracy.

As the kernel functions are given in Eqs. (3.9), (3.10), (3.15) and (3.16), the displacement kernel T_{ij} contains (1/r) term and ln(r) terms, which are singular when the distance r approaches zero. Because of existence of these two singular terms, the integrals on a typical element Γ,

$$\int_{\Gamma} T_{ij}(p,Q)u_j(Q)d\Gamma(Q) \tag{3.23}$$

and,

$$\int_{\Gamma} U_{ij}(p,Q)t_j(Q)d\Gamma(Q) \tag{3.24}$$

are called weakly (the Logarithm type) and strongly singular integrals, respectively. In the modeling of thin structures in the micro or nanoscale by BEM, one possible way is to evaluate them by singularity subtraction and nonlinear coordinate transformation [14].

3.6.1 Regularise nearly-singular integral by singularity subtraction:

Rewriting Eq. (3.23) in the following form:

$$\begin{aligned}\int_{\Gamma} T_{ij}(p,Q)u_j(Q)d\Gamma(Q) = &\int_{\Gamma} T_{ij}(p,Q)\left[u_j(Q)-u_j(Q_o)\right]d\Gamma(Q) \\ &+u_j(Q_o)\int_{\Gamma} T_{ij}(p,Q)d\Gamma(Q)\end{aligned} \tag{3.25}$$

where, Q_o is the closest point on Γ to p Fig. 3.3. As Q → Q_o, the term $\left[u_j(Q)-u_j(Q_o)\right]$ has the order of O(r') where $r=\overline{Q_oQ}$. Then the order of the first integral of right hand side in Eq. (3.35) reduced to O(r')/O(r). This integral is

nearly weakly singular when e is very small. The last integral on right hand side of Eq. (3.25) can be evaluated using the function value at the two end points as:

$$\int_{\Gamma} T_{ij}(p,Q)u_j(Q)d\Gamma(Q) = C_1C_2\left(e_{1i}e_{2j} - e_{2i}e_{1j}\right)\ln r\Big|_{r_1}^{r_2}$$
$$+C_1\{C_2\delta_{ij}\theta + \delta_{1i}\delta_{1j}(\theta + \frac{1}{2}\sin 2\theta) - \frac{1}{2}\left(\delta_{1i}\delta_{2j} + \delta_{2i}\delta_{1j}\right)\cos 2\theta \tag{3.26}$$
$$+\delta_{2i}\delta_{2i}(\theta - \frac{1}{2}\sin 2\theta)\}\Big|_{\theta_1}^{\theta_2}$$

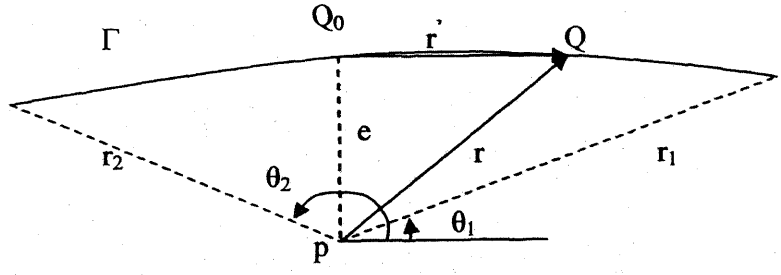

Fig. 3.3: Source point near to the line Γ of integration

For calculation of the first term the natural coordinate system $\xi \in [-1,1]$ is being used and the coordinate ξ is as shown in Fig. 3.4. Then in natural coordinate system,

$$r' = \xi, \qquad r = \sqrt{\xi^2 + e^2} \tag{3.26}$$

For clarity, the following integral is discussed in brief,

$$\int_{\Gamma} \frac{r'}{r} d\Gamma = \int_{-1}^{1} \sqrt{\frac{\xi^2}{\xi^2 + e^2}} d\xi \tag{3.27}$$
$$= \int_{-1}^{0} \sqrt{\frac{\xi^2}{\xi^2 + e^2}} d\xi + \int_{0}^{1} \sqrt{\frac{\xi^2}{\xi^2 + e^2}} d\xi$$
$$= 2\int_{0}^{1} \sqrt{\frac{\xi^2}{\xi^2 + e^2}} d\xi$$

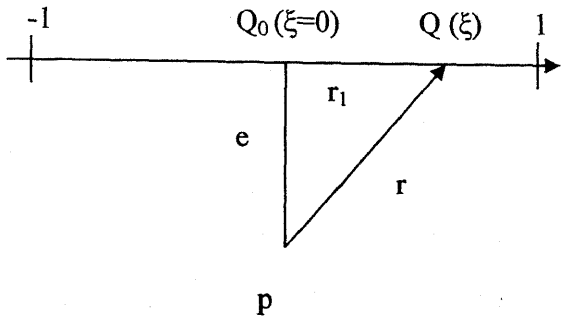

Fig. 3.4: Element Γ in natural coordinate system

Now, let $\xi = \eta^m (m > 2)$, than the above equation reduces to:

$$2\int_0^1 \sqrt{\frac{\xi^2}{\xi^2+e^2}}\,d\xi = 2\int_0^1 m\eta^{m-1}\sqrt{\frac{\eta^{2m}}{\eta^{2m}+e^2}}\,d\eta \tag{3.28}$$

$$= 2\int_0^1 m\sqrt{\frac{\eta^{4m-2}}{\eta^{2m}+e^2}}\,d\eta$$

where m is the order of nonlinear coordinate transformation. When m is large enough, the first integral of right hand side of Eq. (3.25) can be evaluated accurately. For quadratic elements, when e is on 10^{-6} scale or smaller, m = 6 is accurate enough. But best result can be obtained when m lies between 12 to 14 using 10-20 gauss points.

3.6.2 Evaluation of nearly weakly singular integral:

In 2-D elasticity problems, the weakly singular integrals given in (3.24) contain the singular term ln(r). In the singular case, if r = 0, a special logarithmic Gaussian quadrature can be employed. However, when r is very small but not zero, this nearly weakly-singular integral can cause difficulties in the 2-D BEM procedure. Similar nonlinear coordinate transformation as developed in the previous section is used to evaluate the nearly weakly-singular integrals accurately.

Considering the natural coordinate system ξ again, with nonlinear transformation $\xi = \eta^m$, the integration of the term in Eq. (3.24) can be written as:

$$\int_\Gamma \ln r d\Gamma = 2\int_0^1 \frac{1}{2}\ln(\xi^2 + e^2)d\xi \tag{3.29}$$

$$= \int_0^1 m\eta^{m-1}\ln(\eta^{2m} + e^2)d\eta$$

The above integral can be evaluated accurately using a small number of Gauss points when m is large enough.

3.7 *Stress Relaxation:*

The residual stresses at any point inside aluminium layer derived from the previous Sections may exceed the yield limit. Then, these residual stresses will be relaxed either by plastic deformation or by diffusion of voids. The stresses, thus, redistribute themselves according to the temperature profile and material properties locally.

The relaxation of stresses due to diffusion of voids can be taken into account by the use of addition eigenstrain (principle strain) term ε_{ij}^R in the thermal strain [8]. The total eigenstrain ε_{ij}^{**} can be given by,

$$\varepsilon_{11}^{**} = \varepsilon^T + \varepsilon_{11}^R \tag{3.30}$$

$$\varepsilon_{22}^{**} = \varepsilon^T + \varepsilon_{22}^R \tag{3.31}$$

$$\varepsilon_{33}^{**} = \varepsilon^T + \varepsilon_{33}^R = \varepsilon^T - (\varepsilon_{11}^R + \varepsilon_{22}^R) \tag{3.32}$$

where ε^T denotes thermal strain.

Eq. (3.32) is obtained from the condition that the volume of the aluminium line does not change during the relaxation process:

$$\varepsilon_{11}^R + \varepsilon_{22}^R + \varepsilon_{33}^R = 0 \tag{3.33}$$

The stress after relaxation can be calculated from eigenstrains ε_{ij}^{**} as follows:

$$\sigma_{11} = -\frac{\mu}{1-\upsilon}\left(\frac{2+r}{(1+r)^2}\varepsilon_{11}^{**} + \frac{r}{(1+r)^2}\varepsilon_{22}^{**} + \frac{2*\upsilon}{1+r}\varepsilon_{33}^{**}\right) \tag{3.34}$$

$$\sigma_{22} = -\frac{\mu}{1-\upsilon}\left(\frac{r}{(1+r)^2}\varepsilon_{11}^{**} + \frac{r(2r+1)}{(1+r)^2}\varepsilon_{22}^{**} + \frac{2*r*\upsilon}{1+r}\varepsilon_{33}^{**}\right) \tag{3.35}$$

$$\sigma_{33} = -\frac{2\mu}{1-\upsilon}\left(\upsilon\left(\frac{1}{1+r}\varepsilon_{11}^{**} + \frac{r}{1+r}\varepsilon_{22}^{**}\right) + \varepsilon_{33}^{**}\right) \tag{3.36}$$

where r is the aspect ratio of aluminium layer.

Unless the constraint by the surrounding matrix is removed the stresses in the aluminium line can not become zero even after complete relaxation. These stresses can be found in the following manner. The elastic strain energy per unit volume E_o can be expressed as:

$$E_o = -\frac{1}{2}\sigma_{ij}^R \varepsilon_{ij}^{**} \tag{3.37}$$

where the usual summation convention over repeated indices is adopted. From a thermodynamic point of view, the change in the elastic strain energy under a constant temperature is the change in the Helmholtz free energy of the material. Therefore, the relaxation process will proceed until E_o takes it's minimum value. The stresses after complete relaxation can be obtained by applying the energy minimum conditions, i.e.

$$\frac{\partial E_o}{\partial \varepsilon_{11}^{**}} = 0 \text{ and } \frac{\partial E_o}{\partial \varepsilon_{22}^{**}} = 0 \tag{3.38}$$

The equilibrium values of ε_{ij}^R, $\overline{\varepsilon}_{ij}^R$, corresponding to the complete relaxation can be obtained as

$$\overline{\varepsilon_{11}^R} = \frac{(1+\upsilon)[(4r^2-r-2)-2(2r+1)(r-1)\upsilon]}{(2r^2+r+2)-4r\upsilon-2(1-r^2)\upsilon^2}\varepsilon^T \tag{3.39}$$

$$\overline{\varepsilon_{22}^R} = \frac{(1+\upsilon)[-(2r^2-r-2)+2(r+2)(r-1)\upsilon]}{(2r^2+r+2)-4r\upsilon-2(1-r^2)\upsilon^2}\varepsilon^T \tag{3.40}$$

$$\overline{\varepsilon_{33}^{R}} = -\frac{2(1+\upsilon)[(r^2-r+1)-(r-1)^2\upsilon]}{(2r^2+r+2)-4r\upsilon-2(1-r^2)\upsilon^2}\varepsilon^T \tag{3.41}$$

and, the stresses will be

$$\overline{\sigma_{11}^{R}} = \overline{\sigma_{22}^{R}} = \overline{\sigma_{33}^{R}} = \overline{\sigma^{R}} = -6\mu\frac{r(1+\upsilon)}{(2r^2+r+2)-4r\upsilon-2(1-r^2)\upsilon^2}\varepsilon^T \tag{3.42}$$

It is interesting to note that internal stress becomes hydrostatic after the complete relaxation.

3.7.1 Stresses after plastic deformation:

Relaxation by plastic deformation can occur instantaneously by the conservative motion of dislocations. Von Mises or Tresca criteria can be applied to predict the onset of the plastic deformation under the condition of triaxial stresses. For the simplicity of the Tresca criterion, this criterion is being applied here to discuss the plastic relaxation of the aluminium line for 0 < r < 1. According to the Tresca criterion, yielding occurs when

$$\sigma_{33} - \sigma_{22} \geq \sigma_y \tag{3.43}$$

where σ_{33} is largest and σ_{22} is smallest among all the stresses and σ_y is the uniaxial yield stress. The stresses after the plastic relaxation can be evaluated by applying the energy minimum conditions under Tresca criterion. From Eq. (3.43) we have

$$\sigma^P{}_{33} - \sigma^P{}_{22} = \sigma_y \tag{3.44}$$

The superscript P indicated values after plastic deformation. Similarly the relation between $\varepsilon^P{}_{22}$ and $\varepsilon^P{}_{11}$ can be obtained by using Eqs. (3.34) to (3.36) and (3.44), following similar procedure as described for diffusion relaxation, as

$$\varepsilon^P{}_{22} = C_1 + C_2\varepsilon^P{}_{11} \tag{3.45}$$

where

$$C_1 = \frac{(1+r)^2}{4r^2(1-\upsilon)+r(5-4\upsilon)+2}\left(\frac{2(1+\upsilon)}{1+r}\varepsilon^T + \frac{1-\upsilon}{\mu}\sigma_y\right)$$

$$C_2 = \frac{2(1+r)^2(1-\upsilon)+r}{4r^2(1-\upsilon)+r(5-4\upsilon)+2}$$

From the minimum condition, $\frac{\partial E_o}{\partial \varepsilon_{11}^P} = 0$, ε_{11}^P can be obtained at the end of the relaxation by plastic deformation as:

$$[C_2(2C_3 + C_2C_5) + C_4]\varepsilon_{11}^P + (C_6 + C_2C_7)\varepsilon^T + C_1(C_3 + C_2C_5) = 0 \qquad (3.46)$$

where C_3 to C_7 are

$$C_3 = \frac{2r^2(1-\upsilon)+r(5-4\upsilon)+2(1-\upsilon)}{(1+r)^2}$$

$$C_4 = \frac{2r^2(1-\upsilon)+r(5-4\upsilon)+4(1-\upsilon)}{(1+r)^2}$$

$$C_6 = -\frac{2r(1+\upsilon)}{(1+r)}$$

$$C_7 = -\frac{2(1+\upsilon)}{(1+r)}$$

ε_{11}^P is calculated from Eq. (3.46). ε_{22}^P can be calculated from Eq. (3.45) with ε_{11}^P. ε_{33}^P can be obtained from

$$\varepsilon_{33}^P = -\left(\varepsilon_{11}^P + \varepsilon_{22}^P\right) \qquad (3.47)$$

The stress field after the plastic relaxation can be solved by putting above calculated eigenstrain into equations (3.34) to (3.36).

In this section it has been found out that the internal stress σ_{ij}^T can, in principle, be reduced to $\bar{\sigma}_R$ if the complete relaxation is possible. As the relaxation process can occur either by the plastic deformation of aluminium or by the diffusional atom movement of aluminium. However, at low temperatures

where the diffusional relaxation is practically inoperative, only the relaxation by plastic deformation can take place [6]. So, the stress relaxation by complete relaxation can be neglected at low temperatures since it will be of very low order.

3.8 Closure:

In this Chapter, the thermal stress formulation has been explained briefly. Modification in the kernels due to the thin multilayer structure application has also been presented. Stress relaxation by plastic deformation has also been modelled.

Chapter 4

THERMAL GROOVING

Recent works have revealed that stress-induced migration causes serious damage to the aluminium conductor. The failure caused by thermal stresses is classified into two types depending upon the temperature. (1) Low-temperature failure: (at temperature lower than 273 K) the cyclic stress leads to fatigue fracture. (2) High-temperature failure: (at temperature higher than 373 K) the stress causes motion of aluminium atoms and the diffusion causes micro defects.

In this chapter, a stress-induced migration, i.e. diffusion along the surface and grain boundary is being modelled. In addition, the model is further modified to define a fracture criterion so that it can be useful for prediction of time to failure. The effect of the stress concentration near the crack tip is also modelled using empirical relations.

4.1 Introduction:

Aluminium when deposited on a surface followed by cooling forms a polycrystalline structure; the size of the grains thus formed depends on the growth conditions. Fig. 4.1a shows an ideal section of such a grain boundary-surface intersection. The exact shape of the groove is determined by the balance of local thermodynamic forces (the two surface tensions and the grain boundary tension) requiring an equilibrium angle of ψ, as it shown in Fig. 4.1b. With the development of the groove, ridges are also formed on the surface lying on either sides of the interface. These ridges try to flatten by surface diffusion; however this flattering process affects the equilibrium angle and makes the groove to deepen (Fig. 4.1c). Here, this situation is prior to deposition of the passivation

coating so that there are no residual stress along aluminium layer, thus as a result there is no atomic flux along the grain boundary. The groove developed in this way will initially grow very fast and then slows down to reach an equilibrium situation in a period of few hours. This process is known as thermal grooving phenomenon [8].

Thermal grooving alone, therefore, does not cause the failure in the aluminium line by itself, but it provides an early nucleus for grain boundary cracking when wire is subjected to high stress levels. The stress perpendicular to the grain boundary activates the atomic flux along the boundary which enhances the grooving and ultimately resulting in open-circuit failure.

4.2 Estimation of Thermal Grooving:

A typical aluminium conductor in a microelectronic package is shown in Fig 4.2a. In this structure the width of the aluminium layer is so thin that the wire can be considered as a sequence of grains defined by a periodic intergranular boundary which completely traverses the width of the wire. Although the bamboo like structure is effective to prevent electromigration, stress-induced migration inflicts serious damage on the conductor. In the present work a typical layer width of 1 μm is considered which is under a remote tensile stress.

Using the symmetry of the problem, only one quadrant of the groove is analyzed. The initial surface is discretized by a set of N equally spaced points as shown in Fig. 4.2(b).

As explained in reference [4, 7] the key relations to analyze the thermal grooving phenomenon are as follows:

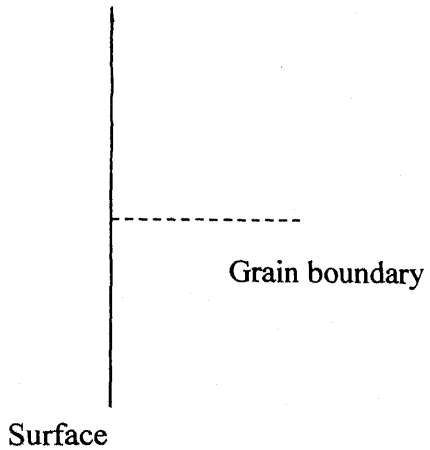

(a) Semi-infinite body with flat surface and grain boundary

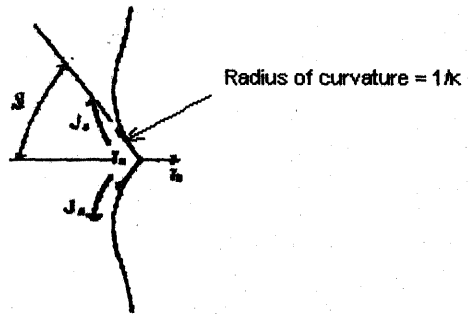

(b) Thermal grooving due to surface diffusion

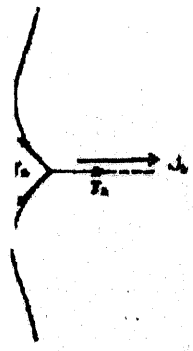

(c) Grain boundary grooving due to combination of diffusion along the surface and that along the grain boundary

Fig. 4.1: Explanation of grooving due to diffusion along the surface and grain boundary

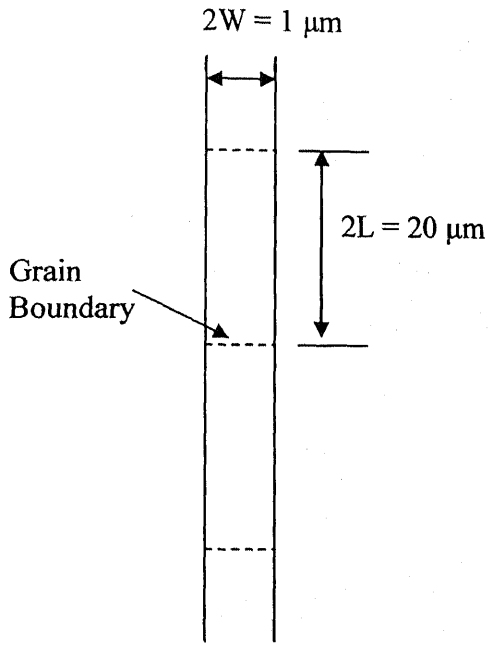

(a) Model conductor with bamboo like structure

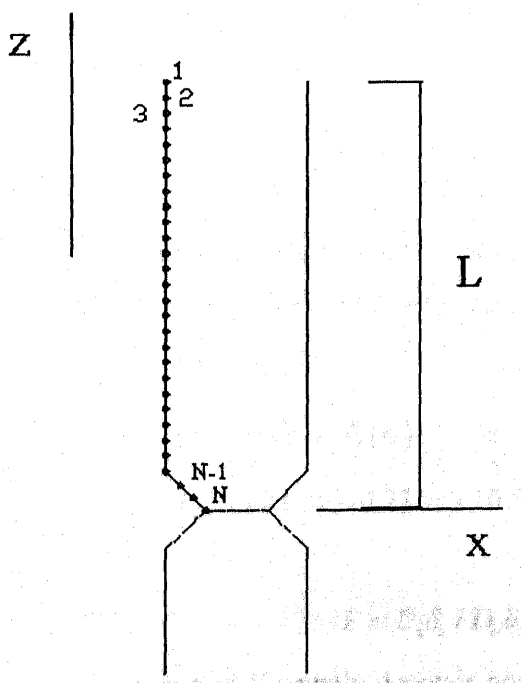

(b) Discritized quadrant of the conductor surface

Fig. 4.2: Modal conductor

The normal velocity of the atoms (Fig. 4.3) at the surface relative to the adjoining solid material can be written as:

$$v_n = -(D_s \delta_s \Omega \gamma_s / kT) \partial^2 \kappa / \partial s^2 \tag{4.1}$$

where, D_s is the surface diffusivity, δ_s is the thickness of diffusion layer, Ω is the atomic volume, γ_s is the surface free energy, k is the Boltzmann constant, T is the temperature, κ is the curvature of the surface, and s is the arc length (Fig. 4.4).

From the equilibrium of the local thermodynamic forces, angle ψ, as shown in Fig. 4.1b, at the interface of the grain boundary and the free surfaces, can be given by:

$$2\gamma_s \cos\varphi = \gamma_b \tag{4.2}$$

where, γ_b is the free grain boundary energy. The curvature at the groove tip, κ_{tip} is defined as [7]:

$$\kappa_{tip} = K_I \sigma_\infty / \gamma_s - (2/3)(1 - a/W) F (\partial\kappa / \partial s)_{tip} \tag{4.3}$$

where K_I is the stress intensity factor in mode-1, σ_∞ is the far field stress, a is the groove depth, W is half width of aluminium layer, and F is diffusion ratio. Stress intensity factor for double-edge-cracked-semi infinite plate under uniform tension can be given as [21]:

$$\begin{aligned} K_I &= \sigma\sqrt{\pi a} \cdot F_1(\alpha), \qquad \alpha = \frac{a}{W} \\ F_1(\alpha) &= 1.12 - 0.231\alpha + 10.55\alpha^2 - 21.72\alpha^3 + 30.39\alpha^4 \end{aligned} \tag{4.15}$$

and,

$$F = D_s \delta_s / D_b \delta_b \tag{4.16}$$

The value of F usually depends not only on the material but also on the temperature and the microstructure of grain boundary and surface. Here, D_b is the grain boundary diffusivity; δ_b is the thickness of diffusion layer at the grain boundary.

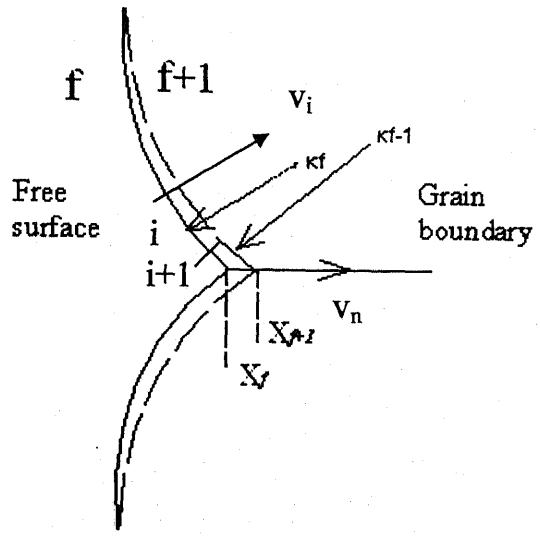

Fig. 4.3: Groove surface profile at time f and f+1

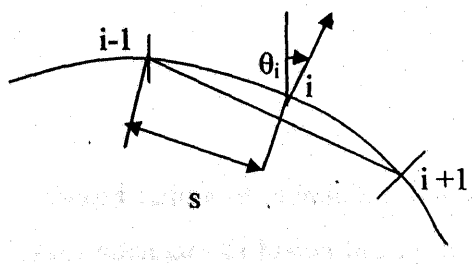

Fig. 4.4: A typical node i subjected to two adjacent elements

Curvature at the other the other nodes can be calculated by the technique given in Appendix 'D'. Using the curvature the velocity at each node can be calculated except the groove tip. The new profile of the groove surface can be calculated by using the velocity at each node. The new coordinate of the groove tip can be obtained by,

$$x_N' = x_{N-1}' + y_{N-1}'/\tan\psi$$
$$y_N' = 0 \tag{4.17}$$

The new and old position of the groove tip can be used to calculate the velocity of the groove tip v_N as follows (Fig. 4.3):

$$v_N = \frac{x_{f+1} - x_f}{\Delta t} \tag{4.18}$$

where Δt is the time step used. The implementation details for the thermal grooving are given in Appendix 'D'.

Some of the assumptions made while deriving the above relations are:

1. Creep cavity growth is uniform along the grain boundary.
2. The properties of the interface are independent of its orientation with respect to the adjacent crystals.
3. The only mechanism operative in the transport of the material is surface and grain boundary diffusion.
4. Effects of the inplane stresses are negligible in thermal grooving process.

4.3 Closure:

In this chapter, stress induced failure of aluminium line at high temperature in terms of surface and grain boundary diffusion has been modelled. To find out stress at the crack tip use of mode-1 stress intensity factor has been made.

Chapter 5

RESULTS AND DISCUSSION

The present BEM method has been applied to perform failure analysis of an Al line of multilevel VLSI circuits. Two ways of failure (plastic flow and thermal grooving) were considered. The failure analysis of the Al interconnectors both during the processing and after the processing is presented here. The results are organized as follows:

1. Failure analysis during processing
2. Thermal grooving

5.1 Validation of the BEM Code:

To validate the BEM code an example problem has been done. In this problem a square plate of silicon with 1mx1m dimensions was considered as shown in Fig. 5.1. A heat flux of 1000 W/m was applied on one of its face. Other faces were left free to dissipate heat by natural convection. The problem was analyzed using the same BEM model discussed in previous Chapters. The transient analysis has done till the structure reached the steady state. Property of the silicon is given in Table 5.1. The results have been validated through finite element software package ANSYS.

The temperature variation at the middle node of the different surface 1, 2 and 3 as shown in Fig. 5.1 is plotted with time in Fig. 5.2. The differences in the three plots are due to the time taken by the heat flux to reach at that location. This plot indicates that initially the temperature increases faster and slows down later. Comparison of the temperature variation with time obtained from the presented BEM technique and finite element software ANSYS at middle point

of surface 1 is shown in Fig. 5.3. The results obtained by the BEM code differs by 1.5% to the results obtained from ANSYS.

Fig. 5.4 shows the temperature profile over the entire domain at steady state. This shows that the temperature is highest at the middle node of surface 1 and lowest at surface 3. It shows that temperature is maximum at the point of application of heat flux and reduces further away from it, which is true qualitatively. Fig. 5.5 shows the temperature variation over entire domain obtained from ANSYS software. The trend of temperature variation over the domain by ANSYS matches with the trend of temperature variation over the domain by BEM code.

Fig. 5.6 shows the total heat flux over entire domain at steady state. Total heat flux is maximum towards the corner of the surface 1 and minimum is at the middle region of surface 3.

5.2 Failure Analysis of Aluminium Line during Processing:

The present analysis is done for a 4-layer printed circuit board (Fig. 5.7). The fabrication process in this work is accomplished in two steps. First, the silicon buffer is covered by borophosphosilicate glass (BPSG) at 673^0C, and cooled to room temperature. In the second step, the 1μm width Al line is formed over the BPSG, and passivated with phosphosilicate glass (PSG). Deposition temperature of the PSG passivation layer was also 673^0C. The complete structure is cooled down to the room temperature. Properties for the above four materials are listed in table 5.1.

The problem is treated in a semi coupled manner: for each time step a thermal analysis is performed, then the resulting temperature profile over the boundary are used for the stress field estimation. Only one half of the domain is analyzed due to the symmetry of the problem. The geometry and the boundary

conditions of a typical multi-level structure are shown in Fig. 5.7. The cooling process is controlled by natural convective boundaries with appropriate values of convective boundaries coefficients. The ambient temperature is assumed to be 25^0C. A typical time step of 0.0001 second is used in the present work. It is assumed that only aluminium has plastic behavior and silicon and glasses are treated as elastic materials. To adequately simulate the large size of the wafer, the silicon wafer used was assumed to be 10 times the thickness of the BPSG, Al and PSG combined. All nodes falling on the line of symmetric are constrained.

Table 5.1: Property data for different layers

	Silicon	BPSG	Aluminium	PSG
E (GPa)	130	120	70	79
ρ (Kg/m^3)	3330	2340	2700	2300
υ	0.28	0.2	0.33	0.2
α	2.3e-06	1.1e-06	23.5e-06	1.1e-06
c_p (J/Kg*K)	712.25	787.5371	904.322	756.471
h (J/m^2*K)	21	4	56	7
λ (J/m*K)	150	10.4	235	12

As explained earlier, the structure is analyzed in two steps:

Step 1: In this step BPSG layer is deposited over the silicon layer at 673^0C and structure is cool down to the room temperature. The discretized domain for step-1 is shown in Fig. 5.8. The cooling curve for the first step is shown in Fig. 5.9. This curve shows that initially the cooling rate is very fast and decreases further as the difference between the layer temperature and atmospheric temperature decreases. It also indicates that the silicon and BPSG layer takes only two seconds to cool down. It was also observed that the temperature profile over entire domain at any instant is quite uniform. This is due to the fact that the

structure is of micro-scale and there is not much difference in temperature of boundary and interior points.

The residual stress σ_{xx}, in the silicon buffer and BPSG layer at the end of Step-1 is shown in Fig. 5.10. It is clear from the stress profile that the silicon layer is under tension while the stress in the BPSG layer is compressive. This is due to the fact that the thermal expansion coefficient of the silicon is almost two times that of BPSG. The stress is varying parabolically along the interface having its peak at the middle of interface.

The residual stress σ_{yy} plot is shown in the Fig. 5.11. It can be seen from the stress profile that the maximum stress is less than that of the σ_{xx}. Further, the σ_{yy} is of tensile nature in the middle region of the interface, while it is of compressive nature towards the either ends of the interface. The residual stress τ_{xy}, plot after step 1 is shown in Fig. 5.12. The stress profile indicates that the τ_{xy} at the interface is of tensile nature towards the free end of the interface, while it is of compressive nature towards the line of symmetry.

The residual stress σ_{zz} plot is shown in Fig 5.13. Comparing the stress distribution of σ_{xx} and σ_{zz}, it can be viewed easily that the stress values σ_{zz} is more.

Step-2: In this step aluminium and PSG layer is formed over the BPSG layer at passivation temperature of 673^0C and full structure is cool down to the room temperature. For Step-2 discretized domain is shown in Fig 5.14. The stress profile calculated from Step-1 is taken as initial stresses for this Step. Fig 5.15 shows the variation of temperature with time at the middle of the.

The residual stress σ_{xx} after deposition of PSG passivation layer and plastic relaxation is shown in Fig 5.16. The stress field obtained shows that the aluminium layer is under tension and the maximum stress lies in the aluminium

line towards the PSG layer. This is due to very high value of thermal expansion coefficient of aluminium with respect to other layers.

Similarly, the residual stress σ_{yy} and σ_{zz} plots after plastic relaxation at the end of step-2 are shown if Fig 5.17 and 5.18, respectively. σ_{yy} is maximum in the aluminium layer while it is of almost zero magnitude at silicon layer. Although there is no thermal and structural analysis performed in the axial direction, the plain stress model used can predict the stress field in this direction also. As shown in Fig. 5.14, the σ_{zz} has values closer to that of σ_{xx} .

5.3 Thermal Grooving:

According to Eq. (5.3) groove growth depends on the axial stresses appearing in the aluminium line. Fig 5.19 shows the charge carrier part of the aluminium line subjected to the σ_{zz}. This plot reveals that the stresses in the axial direction do not very much, so it can be assumed that the far field stress to be constant throughout the aluminium layer. The value of the far field stress used in present work is the average of stresses appearing in aluminium layer. The values of the parameters required to analyze thermal grooving process is listed in Table 5.2. A typical time step of one second is used in the present work.

The modelled groove profile is shown in Fig 5.20. Fig. 5.21 shows that the initial surface profile and the final surface profile at the grain. The final profile here is related with situation when the half width of the aluminium layer is reached by groove tip and this corresponds to the open circle failure of the aluminium layer.

Table 5.2: Property data required to analyze thermal grooving process

γ_s	1.5 J/m^2
$D_b\delta_b$	2.64e-23 m^3/s
Ω	1.66e-29 m^3
k	1.38e-23 J/K
F	100
$\gamma_b/2\,\gamma_s$	1.6

Fig 5.22 is plotted between groove depth and time. Initially groove tip moves faster but slows down as the crack move forward. Fig. 5.23 shows the varation of non-dimensionalized groove depth with nondimensionalized time. The factors used to non-dimensionalize the width, time and stress are given as follows (Section 4.3):

$$\bar{t} = (D_s\delta_s\Omega\gamma_s t)/(kTW^4) \tag{5.1}$$

$$\bar{s} = s/W \tag{5.2}$$

$$\bar{x} = x/W \tag{5.3}$$

$$\bar{a} = a/W, \tag{5.4}$$

and,

$$\bar{v}_n = v_n kTW^3/(D_s\delta_s\Omega\gamma_s), \tag{5.5}$$

where values for all the property data is given in Table 5.2.

Fig 5.24 is plotted between groove growth rates (i.e. velocity at the crack tip) and time. The velocity decrease at the early stages while it becomes constant afterwards. The decrease in growth rate at early stages is governed by the process of thermal grooving due to surface diffusion. Fig 5.25 is plotted between non-dimensional groove growth rates (i.e. non-dimensional velocity at the crack tip) and non-dimensional time.

Fig 5.26 shows that how stress intensity factor is varying with time. It is initially increases faster and it slows down as the crack moves forward.

The time to failure for the aluminium layer as calculated by the analytical model are few seconds [5] while the experiments results have shown that the value of time to failure is typically about hundred hours. The presented numerical method also predicts that the time to failure of aluminium layer is about hundred hours (Fig. 5.27). This is due to the fact that analytical model assumes that grain boundary diffusion process is much faster than surface diffusion (as shown in Fig 5.28), and, under the application of far field stress, grain boundary diffusion control the time to failure. However, the presented numerical method predicts that two processes exist simultaneously, which is more realistic. The two processes are coupled at the groove tip by continuity of chemical potential and atomic flux.

148431

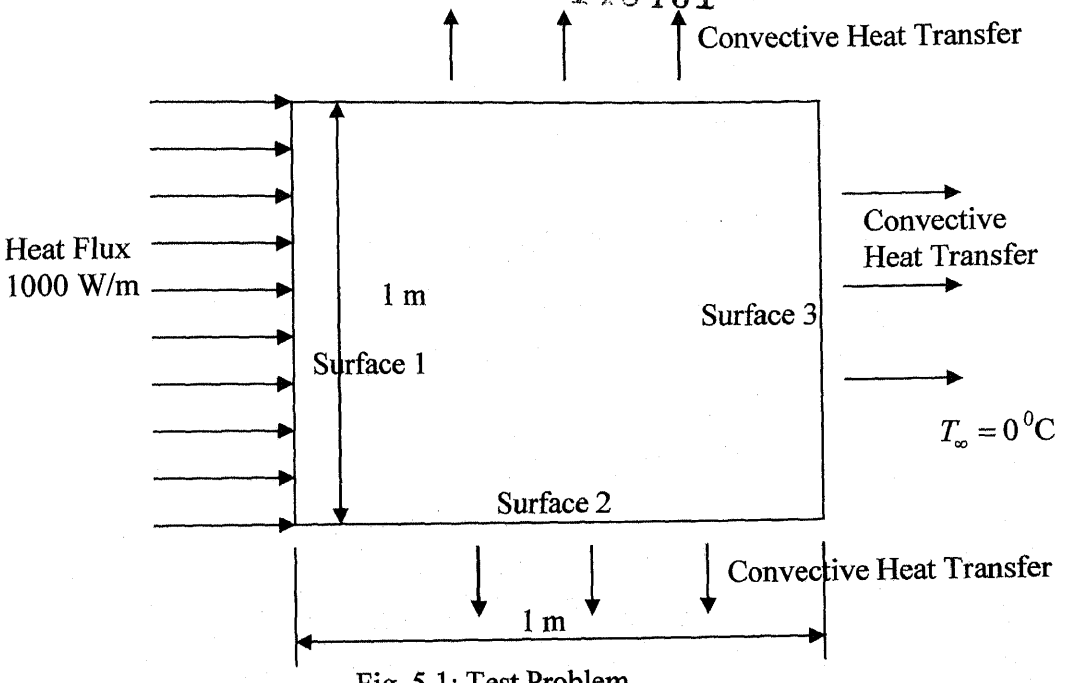

Fig. 5.1: Test Problem

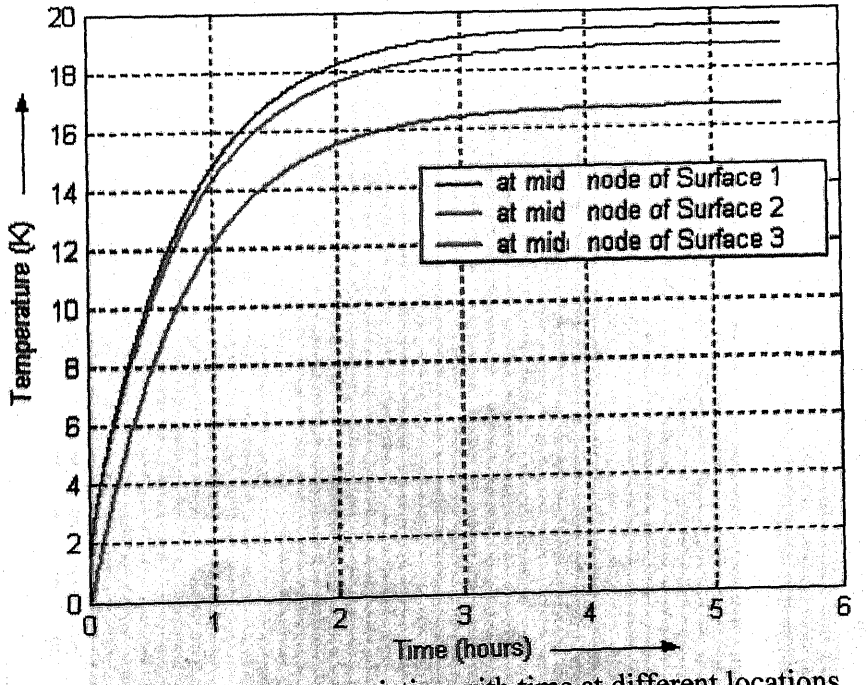

Fig. 5.2: Temperature variation with time at different locations

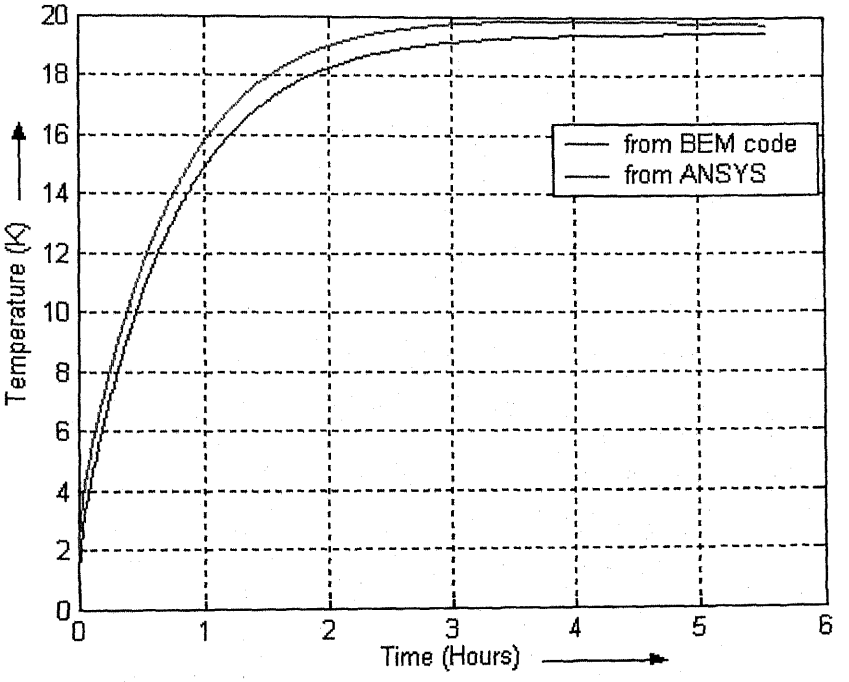

Fig. 5.3: Comparison of the Temperature variation with time by developed BEM code and ANSYS

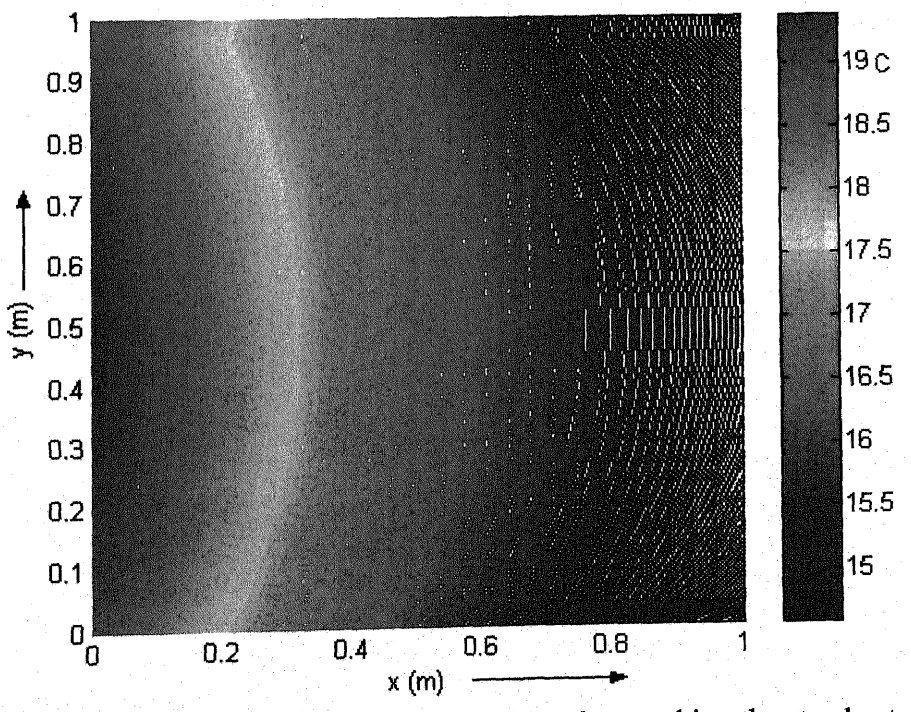

Fig. 5.4: Temperature profile over the domain after reaching the steady state

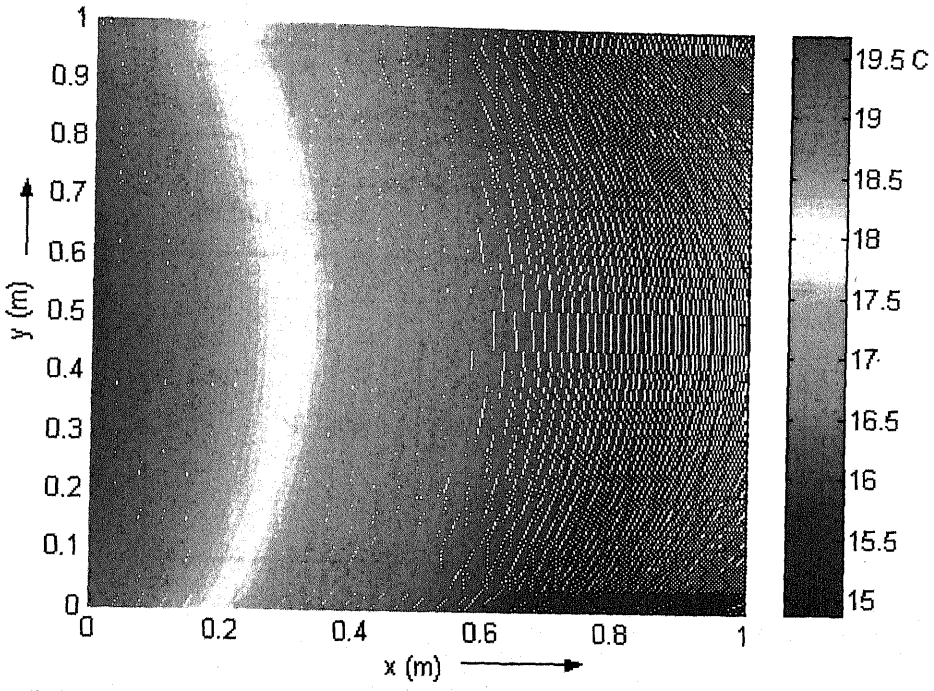

Fig. 5.5: Temperature profile over entire domain at steady state using ANSYS

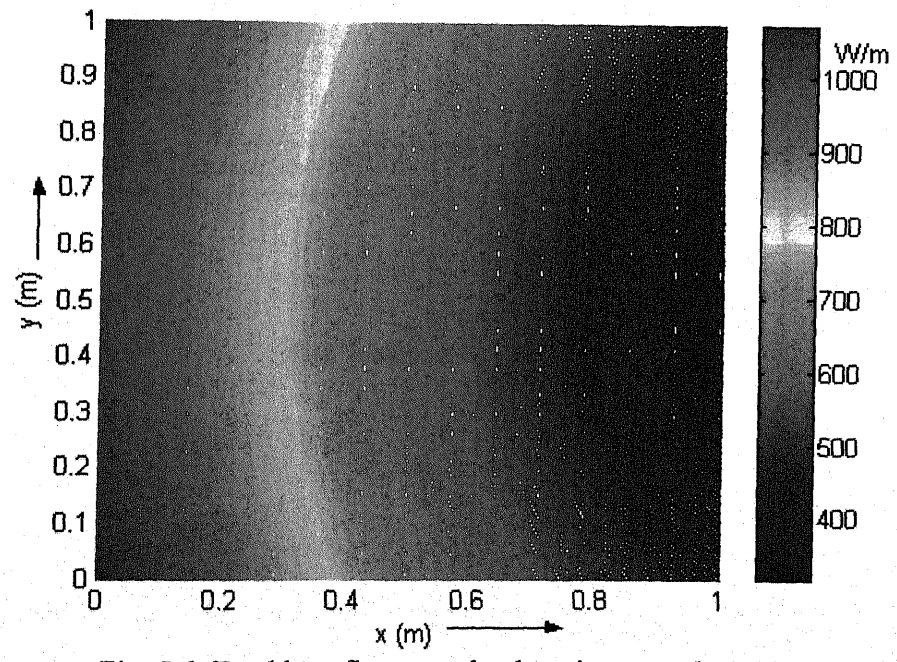

Fig. 5.6: Total heat flux over the domain at steady state

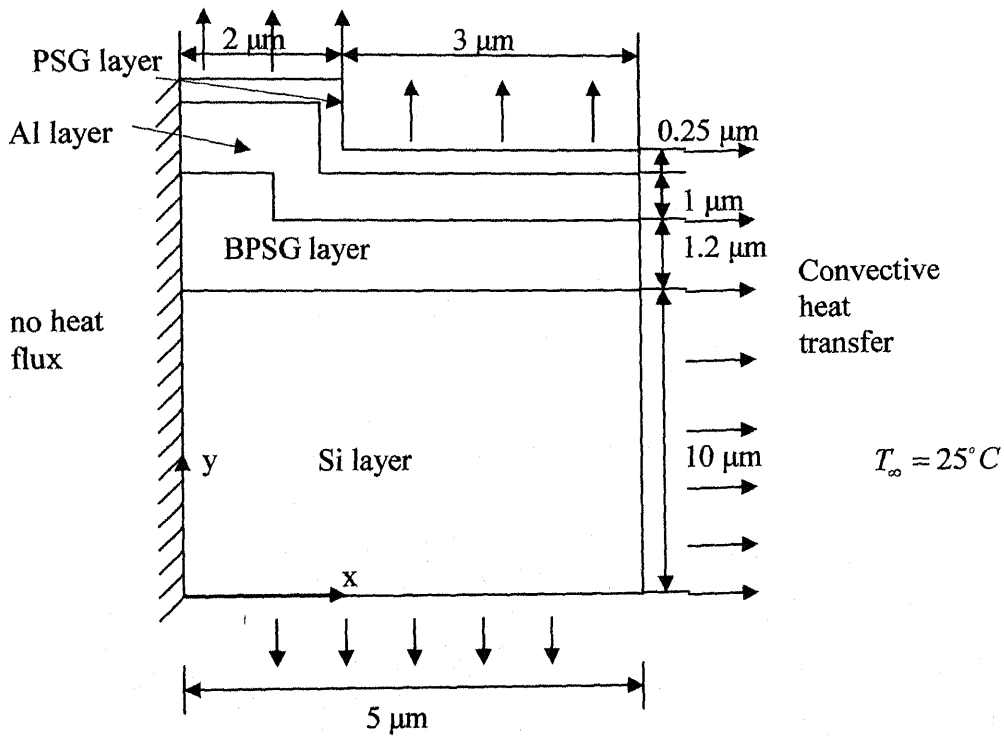

Fig. 5.7: Details of Multilevel Circuit

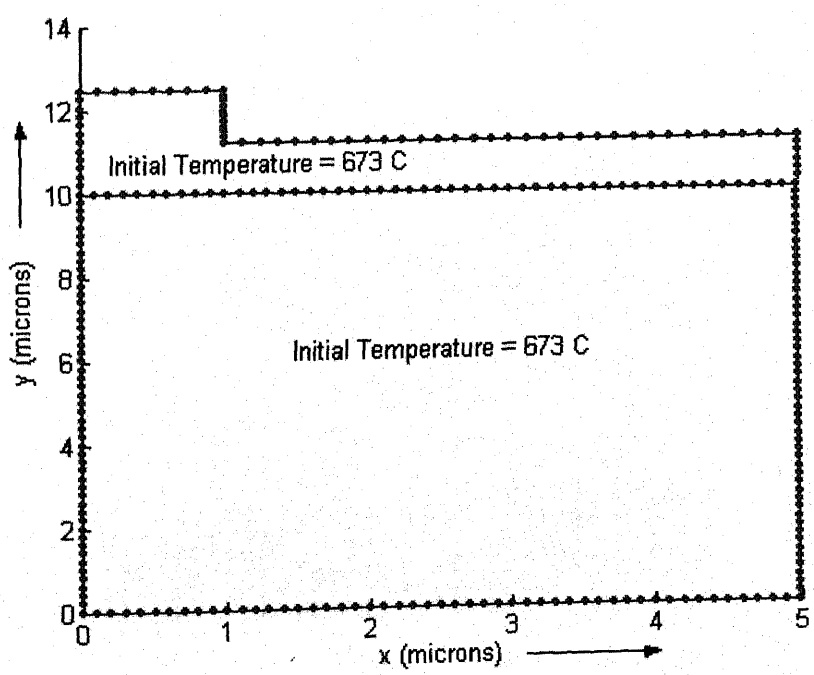

Fig. 5.8: Discritized domain for first step

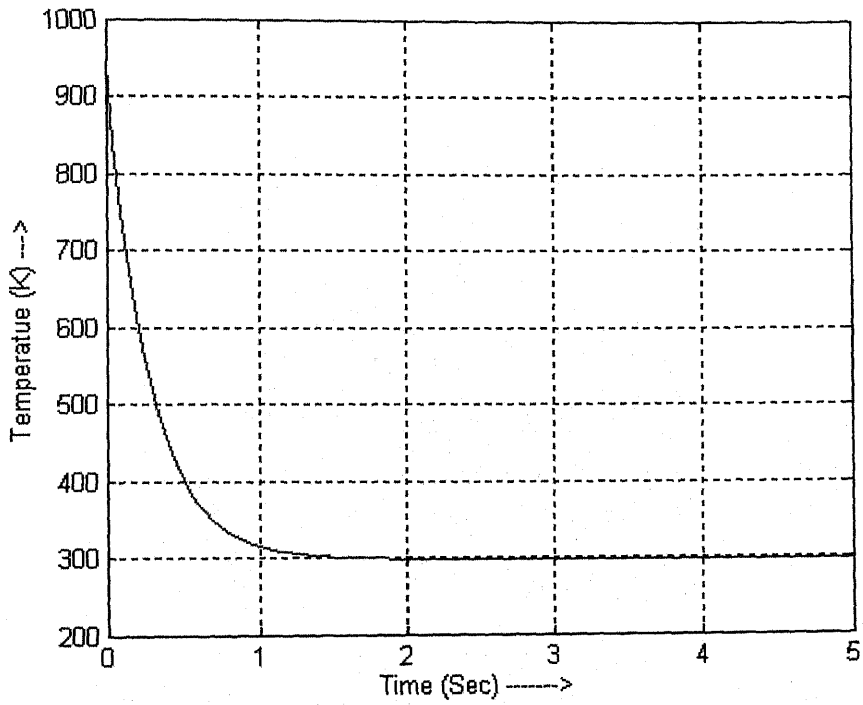

Fig. 5.9: Variation of temperature at mid point of the interface with time

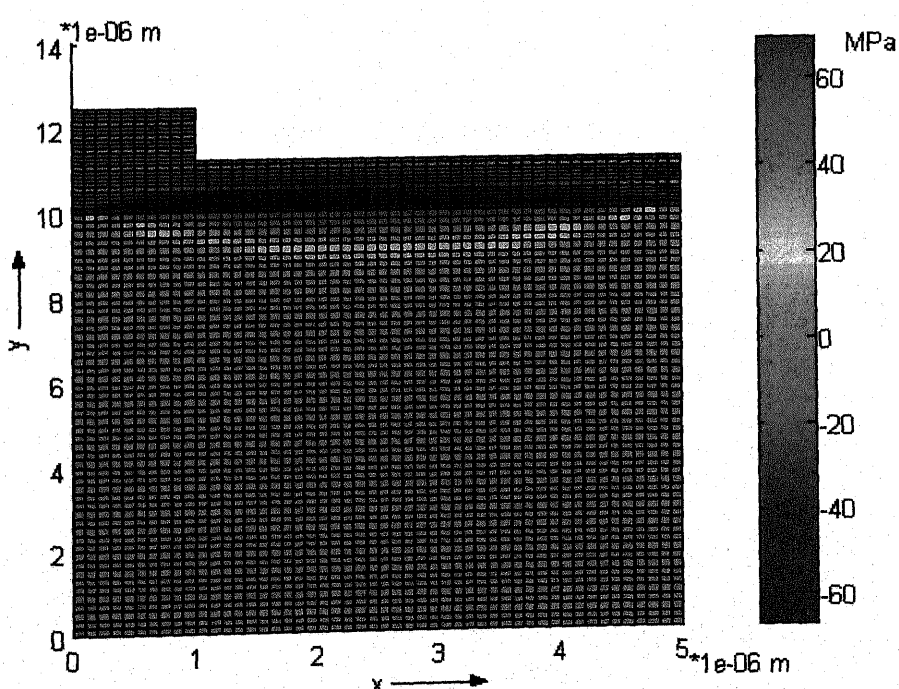

Fig. 5.10: σ_{xx} stress field distribution at the end of first step

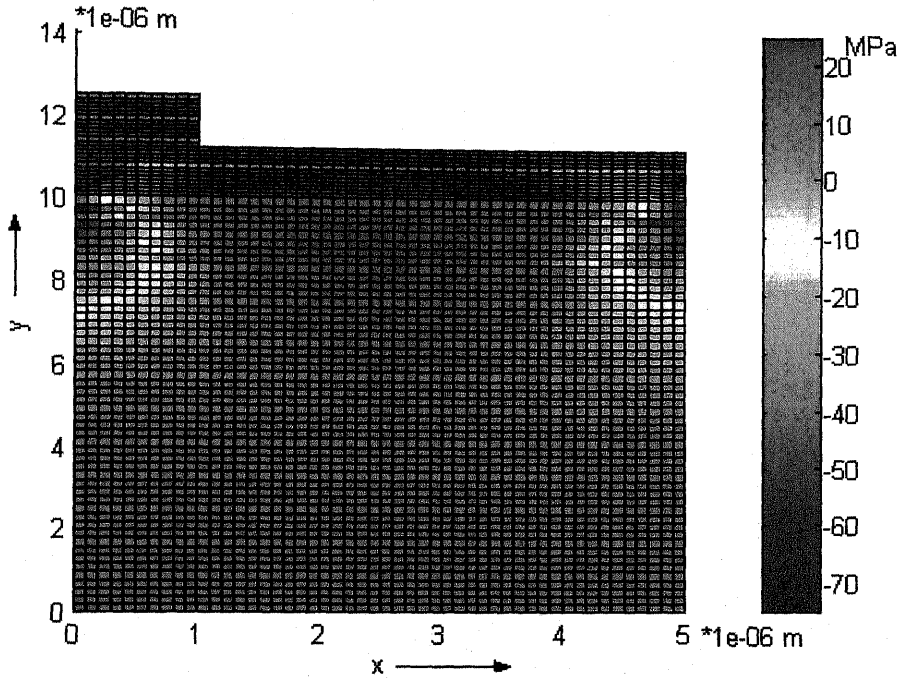

Fig. 5.11: σ_{yy} stress field distribution at the end of first step

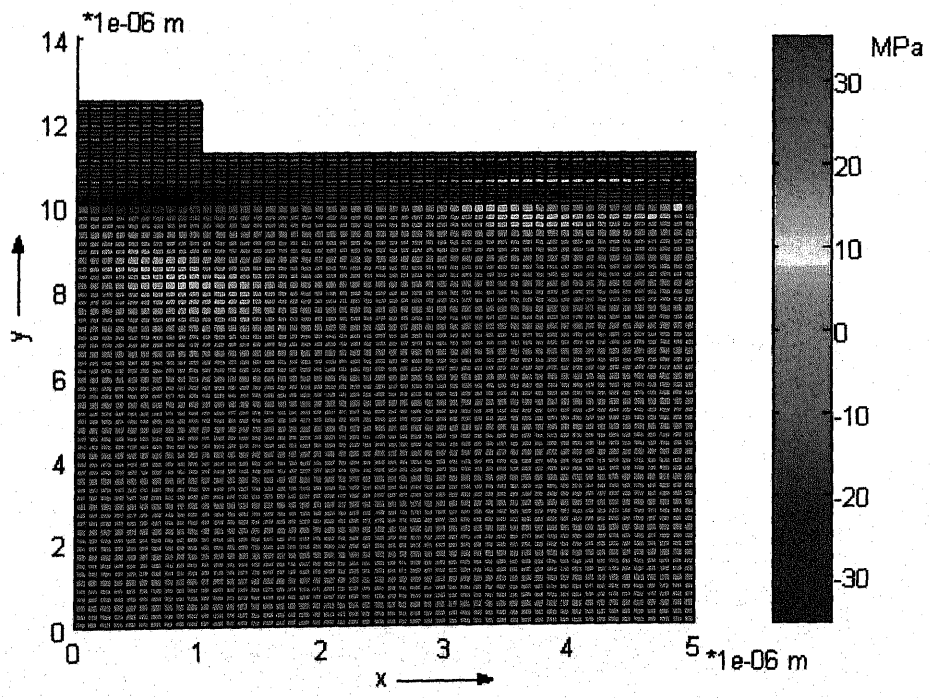

Fig. 5.12: τ_{xy} stress field distribution at the end of first step

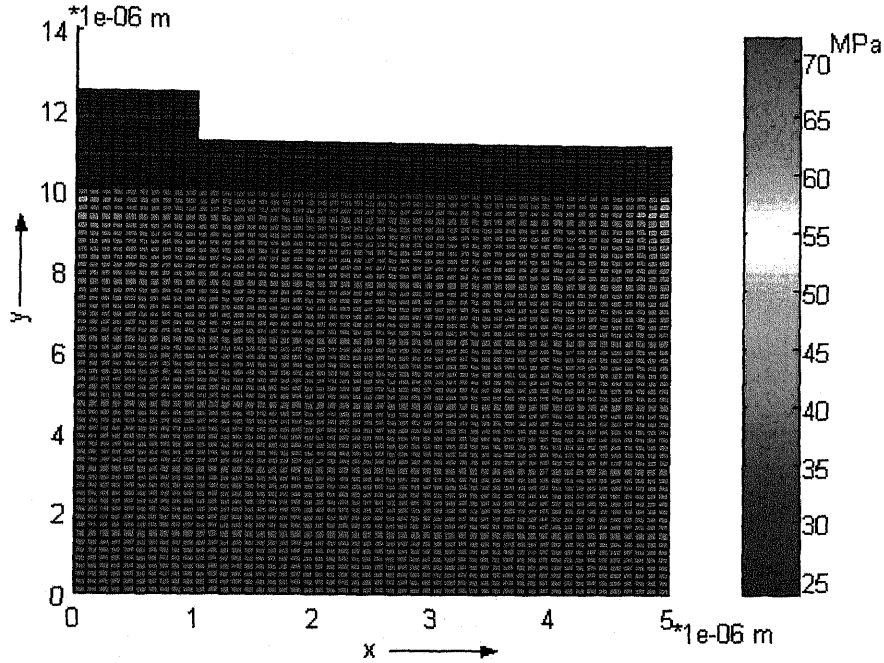

Fig. 5.13: σ_{zz} stress field distribution at the end of first step

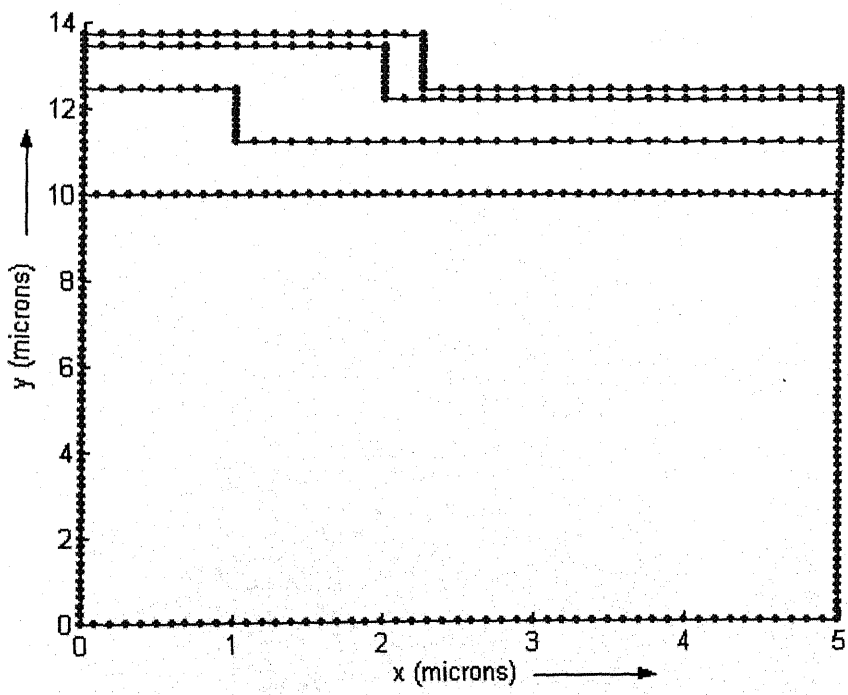

Fig. 5.14: Discritized domain for second step

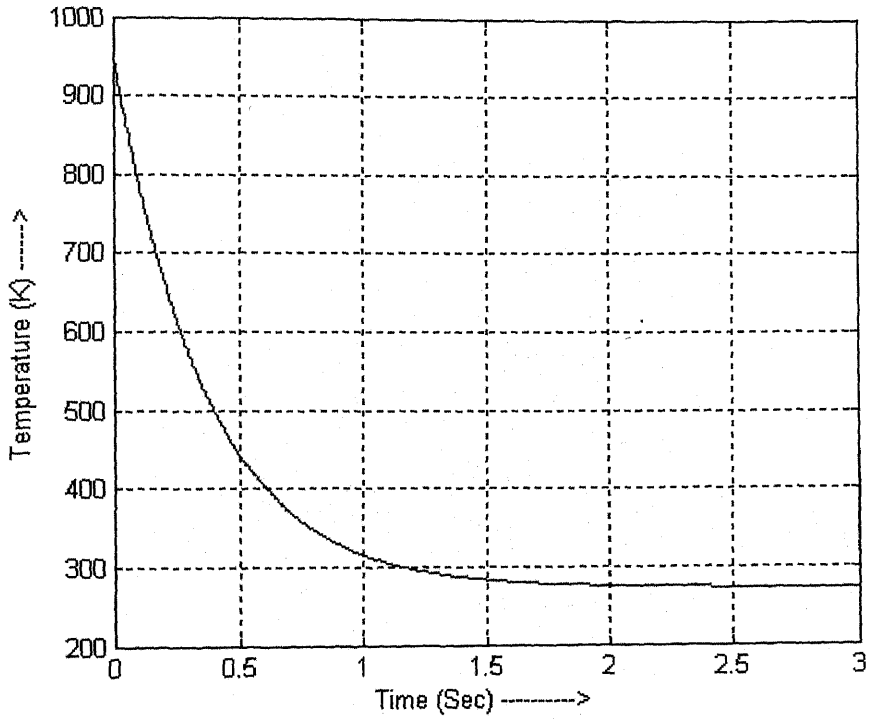

Fig. 5.15: Temperature variation at mid point of aluminium layer with time

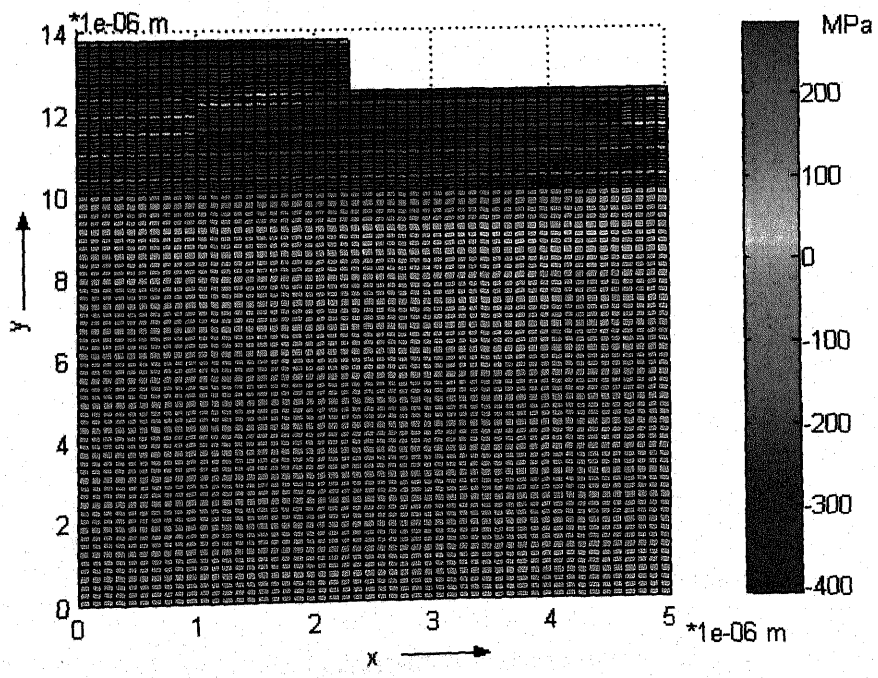

Fig. 5.16: σ_{zz} stress field distribution in the final structure after step 2

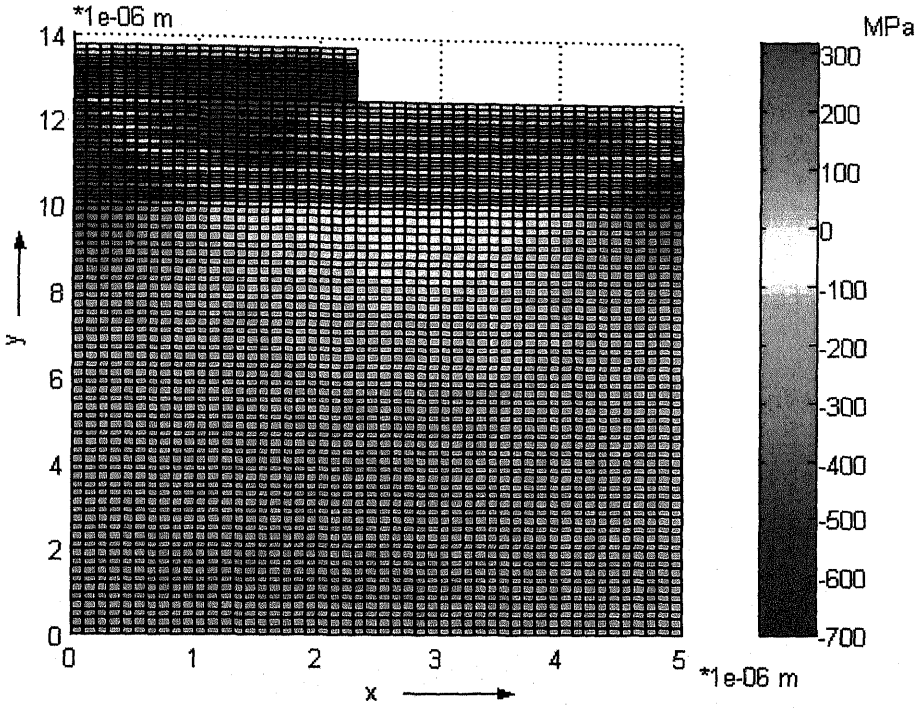

Fig. 5.17: σ_{yy} stress field distribution in the final structure after step 2

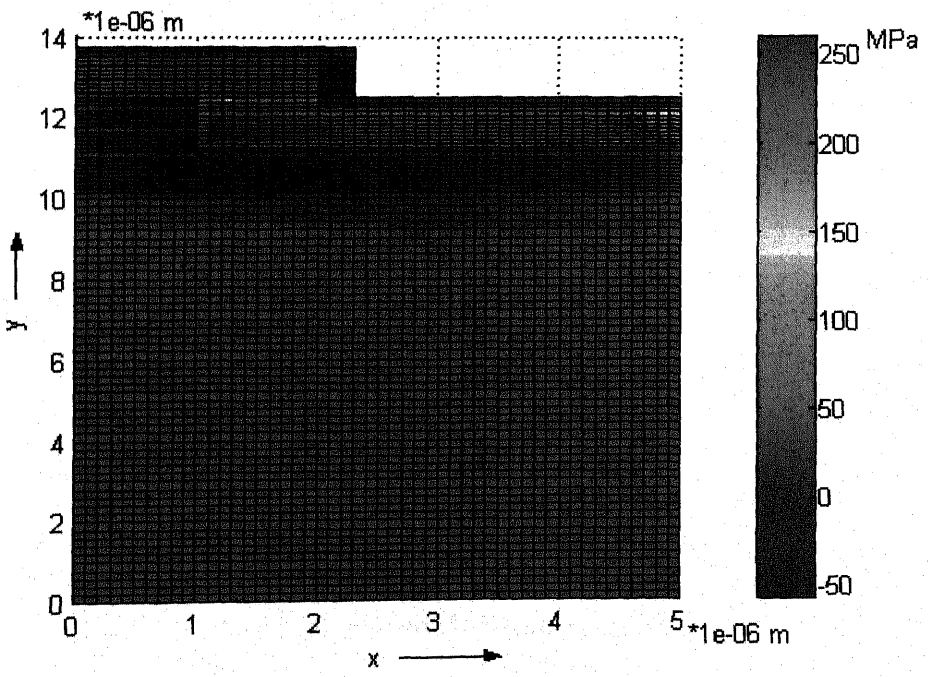

Fig. 5.18: σ_{zz} stress field distribution in the final structure after step 2

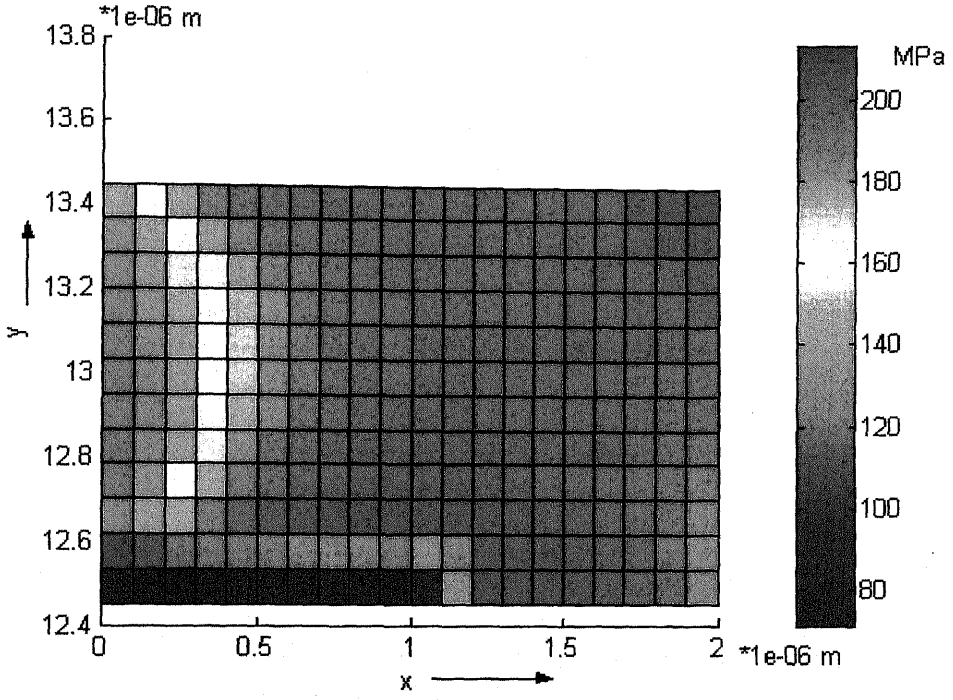

Fig. 5.19: σ_{zz} stress in aluminium layer after step-2

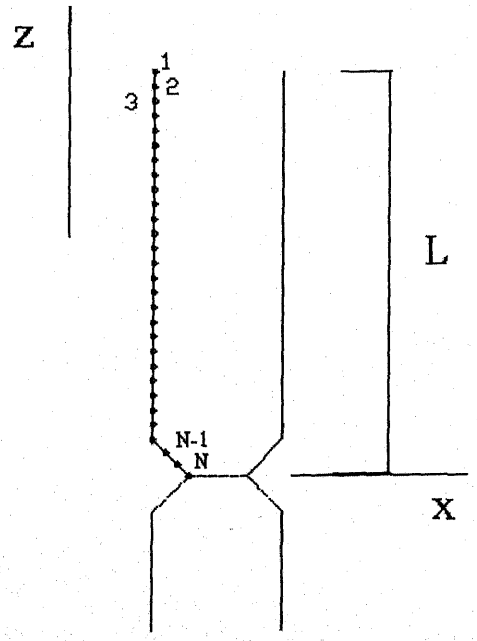

Fig. 5.20: modelled groove profile

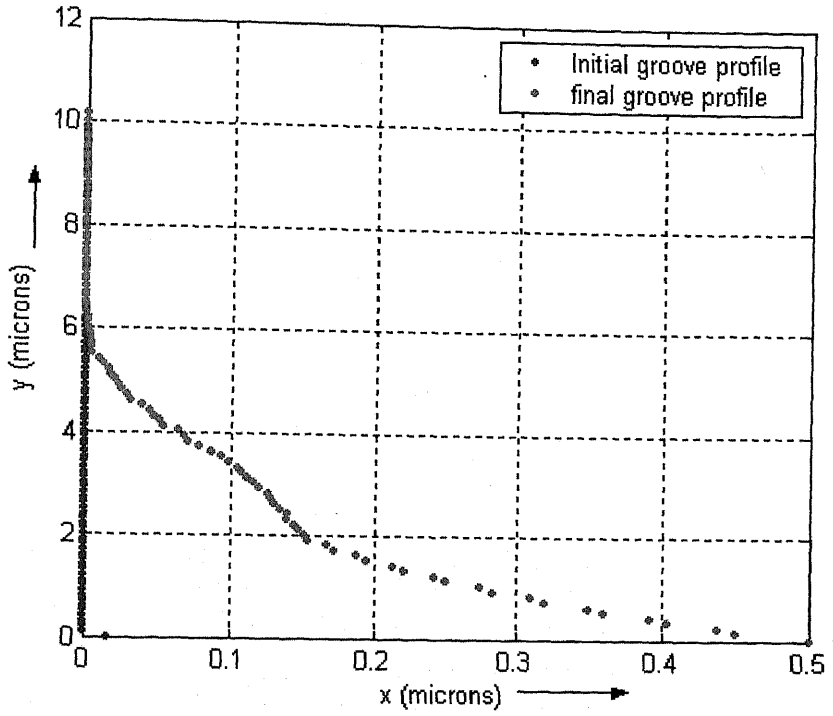

Fig. 5.21: Groove profile; initial profile (blue dots), final profile (red dots)

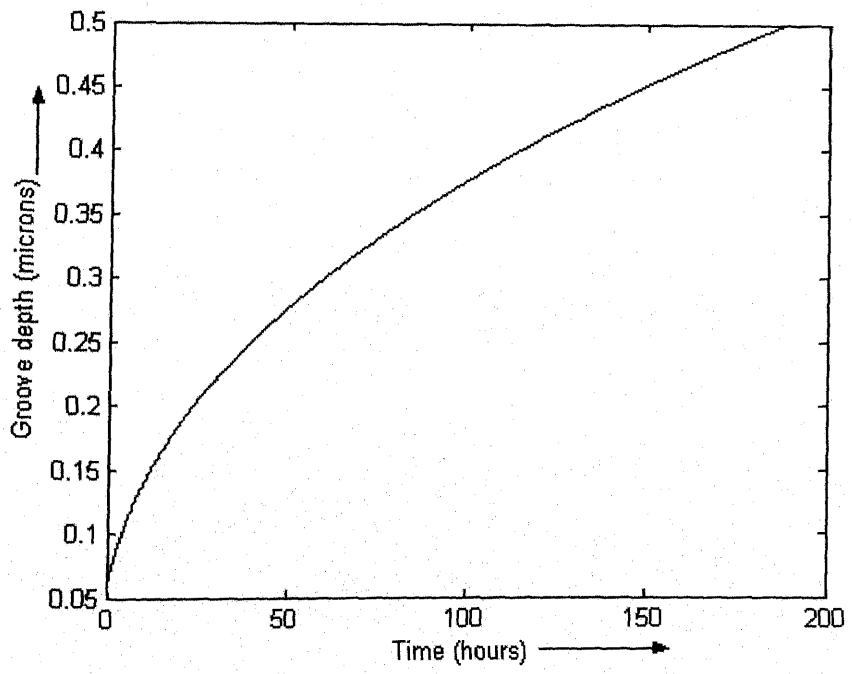

Fig. 5.22: Groove depth with time

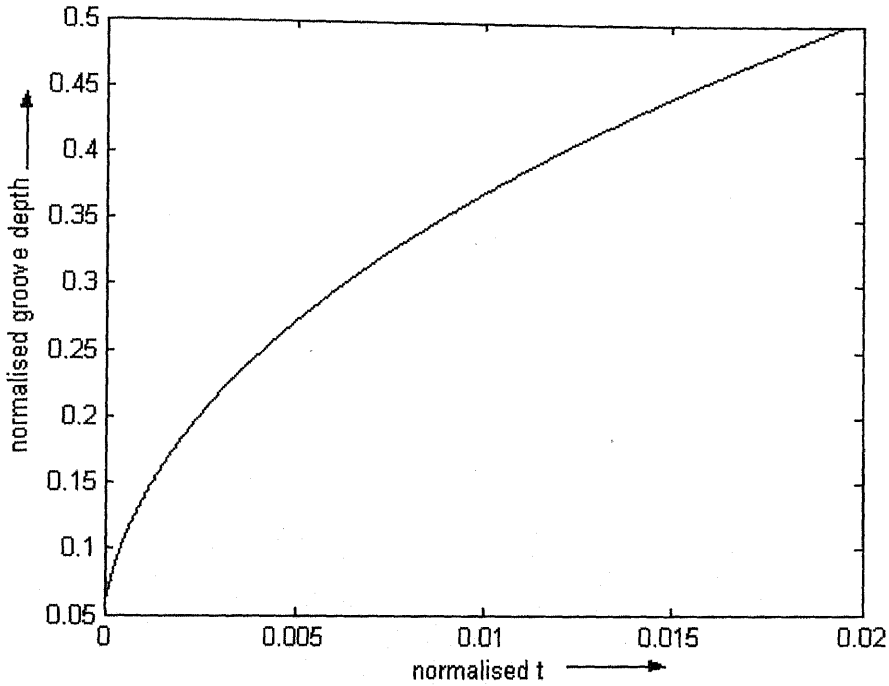

Fig. 5.23: Normalized groove depth Vs normalize time

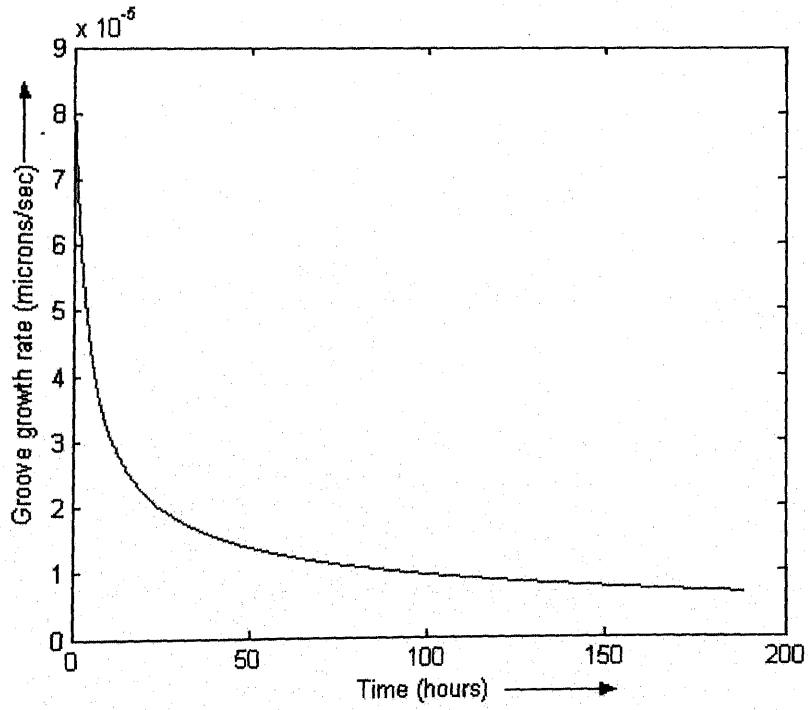

Fig. 5.24: Groove growth rate Vs time

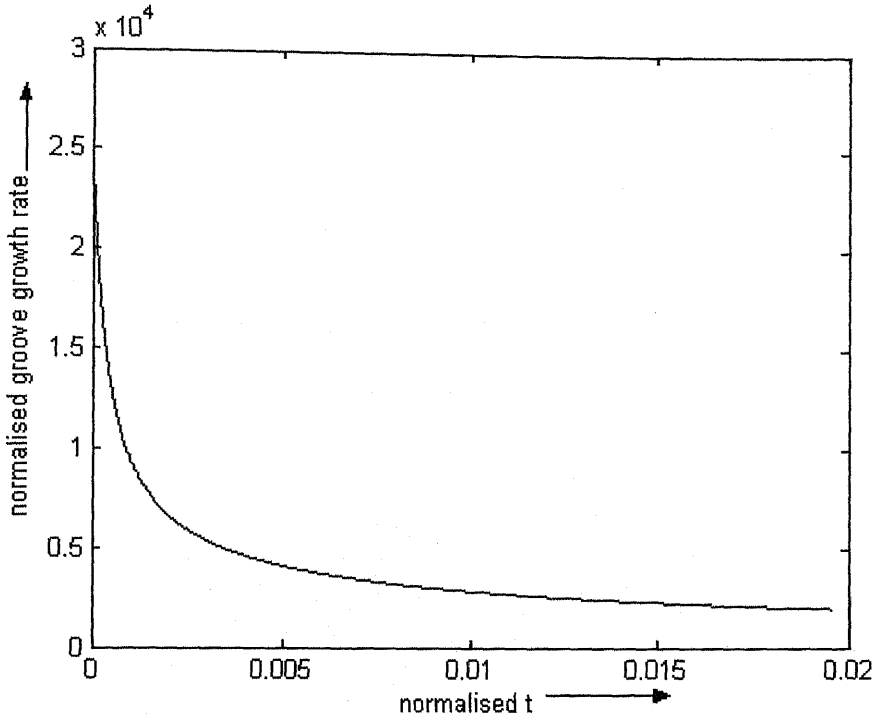

Fig. 5.25: Normalized groove growth rate Vs normalize time

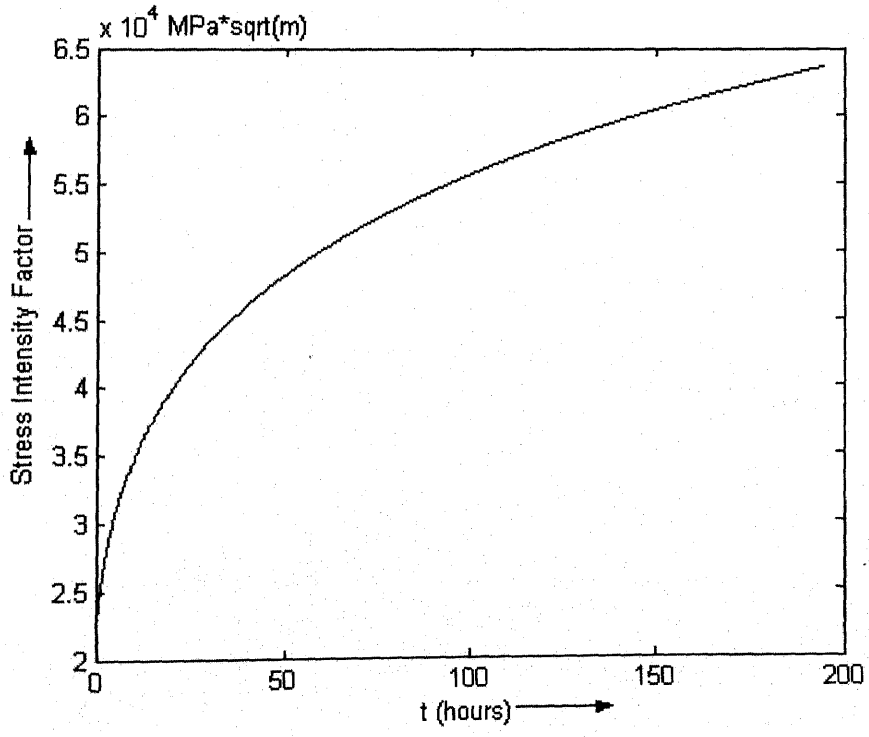

Fig. 5.26: Stress intensity factor Vs normalized time

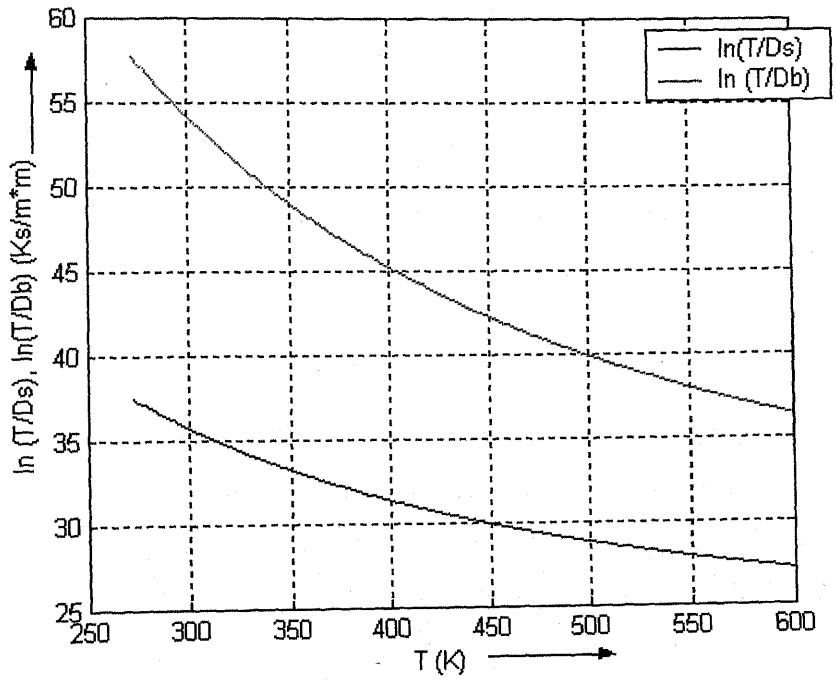

Fig. 5.27: T/D_s and T/D_b Vs temperature

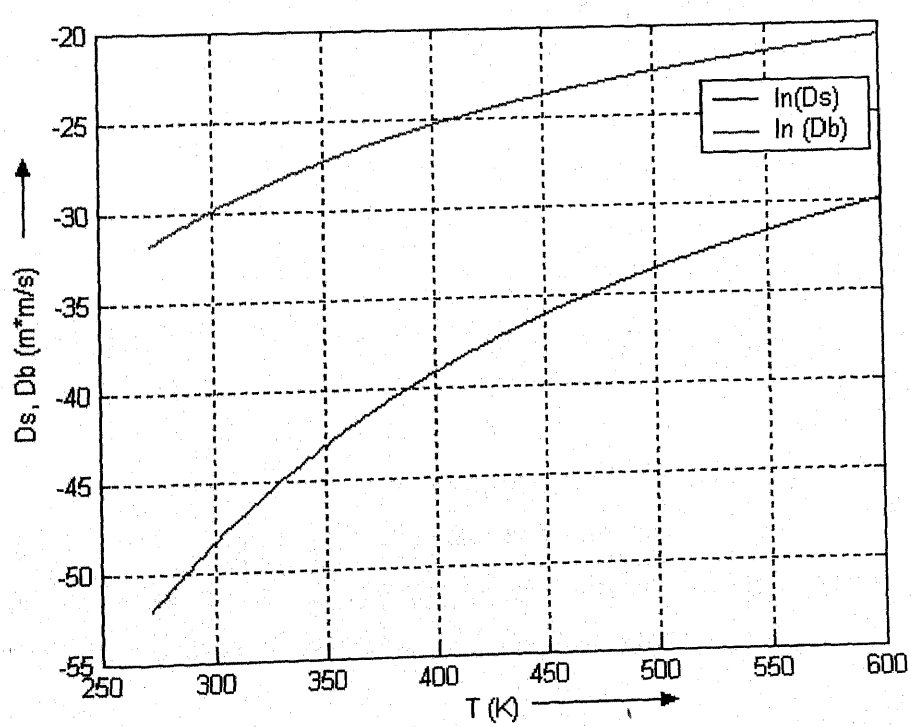

Fig. 5.28: Grain boundary (D_b) and surface (D_s) diffusion coefficients Vs temperature

Chapter 6

CONCLUSIONS AND FUTURE SCOPE

This chapter summarizes the work, and will set forth goals for future work.

6.1 Conclusions

In this work, the residual stress behavior in the aluminium interconnections in a multilevel printed circuit board during processing has been analyzed. Boundary Element method has been used for the purpose with required modifications to calculate the nearly singular integrals accurately in the submicron scale domains. A simplified model for the stress relaxation by plastic deformation has been applied. Stress-migration failure caused by diffusion along the free surface and grain boundary has been modelled accurately. Effect of the stress concentration near the crack tip has been taken care of. The following are the main conclusions drawn from the present work:

- Use of boundary element method is promising in the thin film applications.
- Firstly, a multilevel structure can be modeled step by step, following the manufacturing process.
- In the initial step of fabrication, laying BPSG layer on silicon wafer, σ_{zz} is high at the interface of BPSG and silicon layer.
- In the second step of fabrication, lying passivated aluminum layer on the BPSG layer, σ_{xx} and σ_{zz} are high in the aluminium layer.
- Wherein stress zones near the interface of aluminum and PSG layer are beyond yielding which get relaxed by plastic deformation.

- The surface diffusion is the important mechanism which causes thermal grooving.
- The groove will propagate through half the thickness of aluminum layer in 200 hours causing failure.
- The used step by step technique can be readily extended to more complex situation and material combinations.
- By the use of time dependent fundamental scheme, computation cost gets reduced.
- The result obtained for the thermal grooving give the qualitative agreement with experimental observations.

6.2 Scope for Future Work:

The present work provides some insight to the residual stress behavior and thermal grooving process in aluminium layer of a multilayer printed circuit board. The following work is also of interest and can be pursued as a future work:

- A more realistic model for plastic deformation can be applied.
- Possibility of nucleation and growth of a crack inside aluminium line can be investigated.
- Effect of the any singularity present in silicon wafer like crack, inclusion can be investigated.
- Failure of aluminium line due to electromigration can be investigated.

References:

1. Klema J., Pyle R., Domangue E., *Proc 22nd Relative Physics Symposium IEEE*, Las Vegas, 1984, 1.
2. Curry J., Fitzgibbon G., Guan Y., Mullo R., Nelson G., Thomas A., *Proceedings of 22nd Relative Physics Symposium IEEE*, Las Vegas, 1984, 6.
3. Shen Y. L., "Modeling of thermal stresses in metal interconnects: effect of line aspect ratio", *Journal of Applied Physics*, 82 (4), 1997, 1578-1581.
4. Igic P. M., and Mawby P.A., "An advanced finite element strategy for thermal stress field investigation in aluminium interconnections during processing of very large scale integration multilevel structures", *Microelectronics Journal*, 30 (1999), 1207-1212.
5. Igic P. M., and Mawby P. A., "Investigation of the thermal stress field in a multilevel aluminium metallization in VLSI systems using finite element modeling approach", *Proc. 22nd International Conference on Microelectronics (MIEL 2000)*, Vol. 1, 14-17 May, 2000.
6. Mullins W. W., "Theory of thermal grooving", *Journal of Applied Physics*, Vol. 28, No. 3, March 1957, 333-339.
7. Martinez L., and Nix W. D., "A numerical study of cavity growth controlled by coupled surface and grain boundary diffusion", *Metallurgical Transactions A*, Vol. 13A, March 1982, 427-437.
8. Niwa H., Yagi H., Kato M., and Tsuchikawa H., "Stress distribution in an aluminium interconnect of very large scale integration", *Journal of Applied Physics*, 68 (1), 1990, 328-333.

9. Kitamura T., Othani R., and Yamanaka T., "A numerical simulation on stress-induced failure in aluminium conductors of a microelectronic package based on surface and grain boundary diffusion", *JSME International Journal,* Series A, Vol. 36, No. 2, 1993.
10. Igic P. M., and Mawby P. A., "Numerical modeling of stress-induced failure in sub-micron aluminium interconnects in VLSI systems", *Solid-State Electronics,* 43 (1999) 255-261.
11. Banerjee P. K., *The Boundary Elements Methods in Engineering,* McGraw-Hill, New York, 1994.
12. Pina H. L. G., and Fernandes J. L. M., "Three-dimensional transient heat conduction by the boundary element method", *Proceedings of the Fifth International Conference, Hiroshima, Japan, November 1983*, Springer-Verlag, 1983, 135-142.
13. Wrobel L. C., and Brebbia C. A., *Boundary Element Methods in Heat Transfer*, Computational Mechanics Publications, Elsevier Applied Science, 1992.
14. Luo J. F., Liu Y. J., and Berger E. J., "Analysis of two-dimensional thin structure (from micro- to nano-scales) using boundary element method", *Computational Mechanics*, 22 (1998), 404-412.
15. Luo J. F., Liu Y. J., and Berger E. J., "Interfacial stress analysis for multi-coating systems using an advanced boundary element method", *Computational Mechanics*, 24 (2000), 448-455.
16. Kato M., "Diffusion relaxation and void growth in an aluminium interconnect of very large scale integration", *Journal of Applied Physics*, 68 (1), 1990, 334-338.
17. Becker A. A., *The Boundary Element Method in Engineering*, McGraw Hill Book Company, 1992.

18. Chandra A., Chan C. L., and Lim J., "A BEM approach for transient conduction-convection in machining process", *Advances in Boundary Element Techniques,* Springer-Verlag, 1993.
19. Koizumi M, Utamura M., and Kotani K., "Application of BEM to unsteady 3-dimensional heat conduction problems with non-linear boundary conditions", *Proceedings of the Fifth International Conference, Hiroshima, Japan, November 1983,* Springer-Verlag, 1983, 143-152.
20. Beer Garnot, *Programming the Boundary Element Method*, John Wiley and Sons Ltd, 2001.
21. Golberg M., "Boundary Integral Methods-Numerical and Mathematical Aspects", *Computational Engineering*, Vol. 1, Computational Mechanics Publications, 1999.
22. Chang H. L., "Boundary finite element solution of Multi-dimensional heat conduction equations", *Boundary Elements*, Pergamon Press, 1986, 251-258.
23. *Stress Intensity Factor Handbook*, Vol. 1, Committee of Fracture Mechanics, The Society of Material Science, Japan, Pergamon Press.
24. Kumar Prashant, *Element of Fracture Mechanics*, Wheeler Publishing, New Delhi, 1999.

Appendix A

A.1 Evaluation of the Coefficients of Matrices H1, H2, G1, and G2:

It is important to notice that the fundamental solution T^* and its derivative q^* are function of τ; thus, in the linear case, we have that $H1_{i,j,F,f} = H1_{i,j,F',f'}$ if $F - f = F' - f'$, and the same for H2, G1 and G2. This means that these matrices can be stored and reused whenever needed. Thus, for computer efficiency, it is possible to compute and store all these matrices, which depend only on geometry and time step values, and perform several simulations, for instance for different boundary conditions.

For nonlinear problems, such preliminary calculation is not possible since the diffusivity k is temperature dependent. On the other hand, one should avoid recomputing all coefficients for each new time step due to efficiency reasons. This problem can be overcome by the use of $4N^2$ functions, namely $K1_{i,j}$, $K2_{i,j}$, $K3_{i,j}$, $K4_{i,j}$, closely related to the coefficients $H1_{i,j,F,f}$, $H2_{i,j,F,f}$, $G1_{i,j,F,f}$, and $G2_{i,j,F,f}$ but depending only on the product $k\tau$.

A.1.1 Time Integration:

Expressions (2.6) and (2.7) can be written in the condensed form

$$X^* = Cq^* = \frac{1}{(4k\tau)^{s/2+\varepsilon}} \exp^{(-\frac{r^2}{4k\tau})} \qquad \text{(A.1)}$$

with,

$$C = \frac{1}{\Pi^{s/2}} \quad \text{and } \varepsilon = 0 \qquad \text{if } X^* = T^*$$

$$C = \frac{2d}{\pi^{s/2}} \quad \text{and } \varepsilon = 1 \qquad \text{if } X^* = q^*$$

After inverting the order of integration in expressions (2.14) to (2.15), the following time integrals have to be evaluated.

$$I1 = \int_{t_{f-1}}^{t_f} kX^* dt$$

$$I2 = \int_{t_{f-1}}^{t_f} ktX^* dt$$

For the linear case, k is a constant; for the nonlinear one, it is assumed that the time step Δt is sufficiently small for the approximation k = constant between t_{f-1} and t_f to be valid, e.g. $k(t) = k(t_{f-1})$ over Δt_f.

A.1.2 Evaluation of I1:

Substituting the expression for X^*, i.e.

$$I1 = C \int_{t_{f-1}}^{t_t} \frac{k}{(4k\tau)^{s/2+\varepsilon}} \exp^{(-\frac{r^2}{4k\tau})} dt \tag{A.2}$$

and performing the change of variables

$$x = \frac{r^2}{4k\tau} = \frac{r^2}{4k(t_F - t)} \tag{A.3}$$

with

$$dx = \frac{r^2}{4k\tau^2} dt = \frac{x}{\tau} dt \tag{A.4}$$

The integral I1 can be rewritten as

$$I1 = C \int_{x_{f-1}}^{x_t} \frac{k\tau}{(4k\tau)^{s/2+\varepsilon}} \frac{e^{-x}}{x} dx \tag{A.5}$$

Eliminating the product kτ, according to expression 2.20, gives

$$I1 = \frac{C}{4r^{s+2\varepsilon-2}} \int_{x_{f-1}}^{x_t} x^{s/2+\varepsilon-2} e^{-x} dx \tag{A.6}$$

The result of which is

$$I1 = \frac{C}{4r^{s+2\varepsilon-2}} \left[\Gamma\left(\frac{s}{2} + \varepsilon - 1, x \right) \right]_{x_f}^{x_{f-1}} \tag{A.7}$$

where Γ is incomplete Gamma function,

$$\Gamma(n,x) = \int_x^{\infty} \theta^{n-1} \varepsilon^{-\theta} d\theta$$

A.1.3 *Evaluation of I2:*

Substituting the expression for X^*, i.e.

$$I2 = C \int_{t_{f-1}}^{t_t} \frac{kt}{(4k\tau)^{s/2+\varepsilon}} \exp^{\left(-\frac{r^2}{4k\tau}\right)} dt \tag{A.8}$$

and taking into account that $\tau = t_F - t$,

$$\begin{aligned} I2 &= t_F I1 - C \int_{t_{f-1}}^{t_t} \frac{k\tau}{(4k\tau)^{s/2+\varepsilon}} \exp^{\left(-\frac{r^2}{4k\tau}\right)} dt \\ &= t_F I1 - J2 \end{aligned} \tag{A.9}$$

Introducing again the change of variables given by (A.1), the integral J2 becomes

$$J2 = C \int_{t_{f-1}}^{t_t} \frac{k\tau^2}{(4k\tau)^{s/2+\varepsilon}} \frac{e^{-x}}{x} dt \tag{A.10}$$

or, eliminating the product kτ,

$$J2 = \frac{C}{16r^{s+2\varepsilon-4}} \frac{1}{k} \int_{x_{f-1}}^{x_t} x^{s/2+\varepsilon-2} e^{-x} dx \tag{A.11}$$

This gives

$$J2 = \frac{C}{16r^{s+2\varepsilon-4}} \frac{1}{k} \left[\Gamma\left(\frac{s}{2} + \varepsilon - 2, x \right) \right]_{x_{f-1}}^{x_f} \tag{A.12}$$

A.1.4 Evaluation of Γ(n,x):

The following recurrence relation can be used for evaluating the incomplete Gamma function,

$$\Gamma(n+1,x) = n\Gamma(n,x) + x^n e^{-x} \tag{A.13}$$

$$\Gamma(0,x) = E_1(x)$$

$$\Gamma(\frac{1}{2},x) = \sqrt{\pi}\left[1 - erf\left(\sqrt{x}\right)\right]$$

$$\Gamma(1,x) = e^{-x}$$

in which E_1 is the exponential-integral and *erf* the error function.

A.1.4.1 Numerical integration of the H1, H2, G1, and G2:

The final step in the calculation of the coefficients of matrices H1, H2, G1, and G2 is the spatial integration along the boundary elements. Calling

$$z = k\tau = k(t_F - t)$$

It is possible to introduce four functions of z, namely $K1_{i,j}$, $K2_{i,j}$, $K3_{i,j}$, and $K4_{i,j}$ such that

$$\int_{\Gamma_j} I1(T_i^*)d\Gamma = [K1_{i,j}]_{z_f}^{z_{f-1}} \tag{A.14}$$

$$\int_{\Gamma_j} I1(q_i^*)d\Gamma = [K2_{i,j}]_{z_f}^{z_{f-1}} \tag{A.15}$$

$$\int_{\Gamma_j} J2(T_i^*)d\Gamma = \frac{1}{k}[K3_{i,j}]_{z_f}^{z_{f-1}} \tag{A.16}$$

$$\int_{\Gamma_j} J2(q_i^*)d\Gamma = \frac{1}{k}[K4_{i,j}]_{z_f}^{z_{f-1}} \tag{A.17}$$

The preliminary calculation of the above $4N^2$ functions (N: number of boundary nodes), for point distributed between 0 and y_{max}, makes it possible to determine by interpolating the values of $K1_{i,j}$ to $K4_{i,j}$ at y_f, for all f and all pairs i, j, during the resolution procedure.

Thus taking into accounts expressions (2.12) to (2.15), from the definition of I1, and J2:

$$H1_{i,j,F,f} = \frac{1}{\Delta t_f}\left\{(t_f - t_F)\left[K2_{i,j}\right]_{z_f}^{z_{f-1}} + \frac{1}{k}\left[K4_{i,j}\right]_{z_f}^{z_{f-1}}\right\} \tag{A.18}$$

$$\hat{H}2_{i,j,F,f} = \frac{1}{\Delta t_f}\left\{(t_F - t_{f-1})\left[K2_{i,j}\right]_{z_f}^{z_{f-1}} - \frac{1}{k}\left[K4_{i,j}\right]_{z_f}^{z_{f-1}}\right\} \tag{A.19}$$

$$G1_{i,j,F,f} = \frac{1}{\Delta t_f}\left\{(t_f - t_F)\left[K1_{i,j}\right]_{z_f}^{z_{f-1}} + \frac{1}{k}\left[K3_{i,j}\right]_{z_f}^{z_{f-1}}\right\} \tag{A.20}$$

$$G2_{i,j,F,f} = \frac{1}{\Delta t_f}\left\{(t_F - t_{f-1})\left[K1_{i,j}\right]_{z_f}^{z_{f-1}} - \frac{1}{k}\left[K3_{i,j}\right]_{z_f}^{z_{f-1}}\right\} \tag{A.21}$$

The boundary elements employed in the present work are super parametric, i.e. the shape function used to model the geometry are of higher order than the interpolation functions used to represent the functional variation.

For two dimensional problems, the expressions for K1 to K4 are (omitting the subscripts i, j for simplicity):

$$K1 = \frac{1}{4\pi}\int_{-1}^{+1} E_1(x)|J|d\eta \tag{A.22}$$

$$K2 = \frac{1}{2\pi}\int_{-1}^{+1} \frac{d}{r^2}e^{-x}|J|d\eta \tag{A.23}$$

$$K3 = \frac{1}{16\pi}\int_{-1}^{+1} r^2 \left[\frac{e^{-x}}{x} - E_1(x)\right] |J|\, d\eta \qquad \text{(A.24)}$$

$$K4 = \frac{1}{8\pi}\int_{-1}^{+1} dE_1(x)|J|\, d\eta \qquad \text{(A.25)}$$

where η is the natural coordinate and $|J|$ the Jacobian of the transformation from Γ to η, i.e.

$$|J| = \left|\frac{d\vec{\Gamma}}{d\eta}\right|$$

$$J = \sqrt{\left(\frac{dx(\eta)}{d\eta}\right)^2 + \left(\frac{dy(\eta)}{d\eta}\right)^2}$$

Calculation of the off-diagonal coefficients of matrices H1, H2, G1 and G2 involves only regular integrals, for all time levels t_f up to and including the actual time t_F. In this case, it is noted that $\tau = 0$ and $x \rightarrow \infty$ according to (A.1); thus, all integrands in expressions (A.22) to (A.25) become null.

For the diagonal coefficients (i.e. i = j in expressions (A.18) to (A.21)) we have that, for any $t \neq t_F$, there is a singularity in the calculation of K1 at the source point I where $\vec{r} = 0$ (and x = 0). It is possible to remove this logarithmic singularity by a change of variables

$$\eta = |\xi|^{3/2}\,\mathrm{sgn}(\xi)$$

in which sgn(ξ) takes the sign of ξ and the integration limits are not changed. The Jacobian of this transformation is,

$$\frac{d\eta}{d\xi} = \frac{3}{2}|\xi|^{1/2}\,\mathrm{sgn}(\xi)$$

It can be seen that this Jacobian is zero at the singular pointy $\eta = \xi = 0$, thus the new integral is regular and can be evaluated using standard quadrature schemes.

Appendix B

B.1 Fundamental Solution for Steady State Temperature Calculations:

To calculate two dimensional temperature profile over the domain, the governing equation is Laplace's equation, which can be written as:

$$\nabla^2 T = \frac{\partial^2 T}{\partial x^2} + \frac{\partial^2 T}{\partial y^2} = 0 \tag{B.1}$$

which can be recasted in the boundary integral form as follows:

$$c(p)T(p) + \int_{\Gamma} K_1(p,Q)T(Q)d\Gamma(Q) = \int_{\Gamma} K_2(p,Q)\frac{\partial T(Q)}{\partial n}d\Gamma(Q) \tag{B.2}$$

where K_1 and K_2 are the kernels. These kernels can be evaluated as:

$$\begin{aligned} K_1(p,Q) &= \frac{\partial \lambda(p,Q)}{\partial n} \\ K_2(p,Q) &= \lambda(p,Q) \end{aligned} \tag{B.3}$$

where λ is the fundamental solution. λ, for the steady state thermal analysis, can be written as:

$$\lambda(p,Q) = \frac{1}{2\pi}\ln\left(\frac{1}{r(p,Q)}\right) \tag{B.4}$$

Appendix C

C.1 Two-Dimensional Thermo-elastic Kernels:

Temperature variation causes thermal stresses in a domain which causes an extra term to be introduced into the stress tensor as follows:

$$\left[\sigma_{ij}\right]^{(t)} = \left[\sigma_{ij}\right]^{(e)} + \frac{\alpha E}{1-2\beta\upsilon}\phi(Q)\delta_{ij} \tag{C.1}$$

where, the superscript (t) and (e) refer to the thermo-elastic and elastic stresses, respectively. Multiplying the stresses by unit outward normal, $n_j(Q)$, and using the traction definition $t_j(Q) = \sigma_{ij} n_j(Q)$ results in the following expression

$$\left[t_j(Q)\right]^{(t)} = \left[t_j(Q)\right]^{(e)} + \frac{\alpha E}{1-2\beta\upsilon}\phi(Q) n_j \tag{C.2}$$

Substituting this thermo-elastic traction and applying the divergence theorem into the BIE of Eq. (3.8) results in the following integral equation

$$u_i(p) + \int_S T_{ij}(p,Q) u_j(Q) dS(Q) = \tag{C.3}$$

$$\int_S U_{ij}(p,Q) t_j(Q) dS(Q) + \frac{\alpha E}{1-2\upsilon}\int_V \frac{\partial U_{ij}(p,q)}{\partial x_j}\phi(q) dV(q)$$

The above equation is valid for both 2-D and 3- applications. For Convenience, referring the body force integral as:

$$B_i = \frac{\alpha E}{1-2\upsilon}\int_V \frac{\partial U_{ij}(p,q)}{\partial x_j}\phi(q) dV(q) \tag{C.4}$$

Using the expression (3.9) for the two-dimensional kernel U_{ij} the volume integral is now a domain integral and can be expressed in terms of distance as:

$$B_i = \frac{\alpha(1+\upsilon)}{2\pi(1-\upsilon)}\int_A \frac{\partial}{\partial x_j}\left[\ln r(p,q)\right]\phi(q) dA(q) \tag{C.5}$$

where, A is the area of the enclosed domain. In order to achieve the transformation from a domain to a surface integral by using the divergence

theorem, some algebraic manipulation is necessary. The domain integral must be expressed as a differential operator in ∇^2 by using the following expression:

$$\nabla^2\left[r^2(p,q)\ln r(p,q)\right]=4\left[\ln r(p,q)+1\right] \tag{C.6}$$

therefore,

$$\ln r(p,q)=\frac{\nabla^2\left[r^2(p,q)\ln r(p,q)\right]-4}{4} \tag{C.7}$$

Substituting the above integral into domain integral of Eq. (C.5) results in:

$$B_i=\frac{\alpha(1+\upsilon)}{8\pi(1-\upsilon)}\int_A\frac{\partial}{\partial x_j}\left\{\nabla^2\left[r^2(p,q)\ln r(p,q)\right]-4\right\}\phi(q)dA(q) \tag{C.8}$$

rearranging the differential operator,

$$B_i=\frac{\alpha(1+\upsilon)}{8\pi(1-\upsilon)}\int_A\nabla^2\left\{\frac{\partial}{\partial x_j}\left[r^2(p,q)\ln r(p,q)\right]\right\}\phi(q)dA(q) \tag{C.9}$$

The above expression is now convenient for use in Green's second identity, which can be stated as:

$$\int_A\left[\phi(q)\nabla^2\lambda-\lambda\nabla^2\phi(q)\right]dA(q)=\int_\Gamma\left[\phi(q)\frac{\partial\lambda}{\partial n}-\lambda\frac{\partial\phi(q)}{\partial n}\right]\phi(q)d\Gamma(Q) \tag{C.10}$$

where $\Gamma(Q)$ is a line integral. By using the substitution

$$\lambda=\frac{\partial}{\partial x_i}\left[r^2(p,q)\ln r(p,q)\right] \tag{C.11}$$

and, $\nabla^2\phi=0$, the domain integral of Eq. (C.9) can now be transformed into an line integral as follows:

$$B_i=\frac{\alpha(1+\upsilon)}{8\pi(1-\upsilon)}\int_\Gamma\frac{\partial}{\partial n}\left\{\frac{\partial}{\partial x_j}\left[r^2(p,Q)\ln r(p,Q)\right]\right\}\phi(Q)d\Gamma(Q) \tag{C.12}$$
$$-\frac{\alpha(1+\upsilon)}{8\pi(1-\upsilon)}\int_\Gamma\left\{\frac{\partial}{\partial x_j}\left[r^2(p,Q)\ln r(p,Q)\right]\right\}\frac{\partial\phi(Q)}{\partial n}d\Gamma(Q)$$

The above equation contains only surface integrals and that the interior point q has now become a surface point Q. For convenience, the thermo-elastic surface integrals can be expressed as thermo-elastic kernels as:

$$B_i = \int_\Gamma M_i(p,Q)\phi(Q)d\Gamma(Q) + \int_\Gamma N_i(p,Q)\frac{\partial\phi(Q)}{\partial n}d\Gamma(Q) \tag{C.13}$$

Therefore, the two-dimensional thermo-elastic kernels can be written as follows:

$$M_i = \frac{\alpha(1+\upsilon)}{8\pi(1-\upsilon)}\frac{\partial}{\partial n}\left\{\frac{\partial}{\partial x_i}\left[r^2(p,Q)\ln r(p,Q)\right]\right\} \tag{C.14}$$

$$N_i = \frac{-\alpha(1+\upsilon)}{8\pi(1-\upsilon)}\frac{\partial}{\partial x_i}\left[r^2(p,Q)\ln r(p,Q)\right] \tag{C.15}$$

These kernels can be further expanded to

$$M_i = \frac{-\alpha(1+\upsilon)}{8\pi(1-\upsilon)}\left\{\left[2\ln r(p,Q)-1\right]n_i + 2\frac{\partial r(p,Q)}{\partial x_i}\frac{\partial r(p,Q)}{\partial n}\right\} \tag{C.16}$$

$$N_i = \frac{\alpha(1+\upsilon)}{8\pi(1-\upsilon)}r(p,Q)\frac{\partial r(p,Q)}{\partial x_i}\left[2\ln r(p,Q)-1\right] \tag{C.17}$$

Appendix D

D.1 Implementation Details for Thermal Grooving:

The curvature value at any node is found out by approximating a circle at that node and two of its neighboring points. Thus, the magnitude of the curvature, $\bar{\kappa}$ is approximately given by:

$$\bar{\kappa}_i = 1 \Big/ \sqrt{\left(\bar{x}_i - \bar{x}_i^c\right)^2 + \left(\bar{y}_i - \bar{y}_i^c\right)^2} \qquad \text{(D.1)}$$

where $\bar{x}_i^c$ and $\bar{y}_i^c$ are the nondimensionalized coordinates of the center of circle, given by:

$$\bar{x}_i^c = \frac{(\bar{y}_i - \bar{y}_{i+1})\left[\bar{x}_{i+1}^2 + \bar{y}_{i+1}^2 - \bar{x}_i^2 - \bar{y}_i^2\right] - (\bar{y}_{i-1} - \bar{y}_i)\left[\bar{x}_i^2 + \bar{y}_i^2 - \bar{x}_{i-1}^2 - \bar{y}_{i-1}^2\right]}{2\left[(\bar{x}_{i-1} - \bar{x}_i)(\bar{y}_i - \bar{y}_{i+1}) - (\bar{x}_i - \bar{x}_{i+1})(\bar{y}_{i-1} - \bar{y}_i)\right]} \qquad \text{(D.2)}$$

$$\bar{y}_i^c = \frac{(\bar{x}_{i-1} - \bar{x}_i)\left[\bar{x}_i^2 + \bar{y}_i^2 - \bar{x}_{i+1}^2 - \bar{y}_{i+1}^2\right] - (\bar{x}_i - \bar{x}_{i+1})\left[\bar{x}_{i-1}^2 + \bar{y}_{i-1}^2 - \bar{x}_i^2 - \bar{y}_i^2\right]}{2\left[(\bar{x}_{i-1} - \bar{x}_i)(\bar{y}_i - \bar{y}_{i+1}) - (\bar{x}_i - \bar{x}_{i+1})(\bar{y}_{i-1} - \bar{y}_i)\right]} \qquad \text{(D.3)}$$

The velocity of groove is obtained by Eq. (4.1) and the Eqs. (4.2) and (4.3). $(\partial x / \partial s)_{tip}$ can be approximated as $(\bar{x}_N - \bar{x}_{N-1}) / \bar{s}_N$ where $\bar{s}_N$ is the non-dimensional distance between points "N-1" and "N".

The sign of the curvature is found out by drawing a straight line between the anterior and the posterior neighbors of the corresponding points as shown in Fig. D.1; if this point is located at the right of the line, then a positive sign is given to the curvature and vice versa.

As the factors W, $(kTW^4)/(D_s\delta_s\Omega\gamma_s)$, γ_s / W represent the dimension of length, time and stress, respectively, the grooving equation can be normalized on the basis of the following relations:

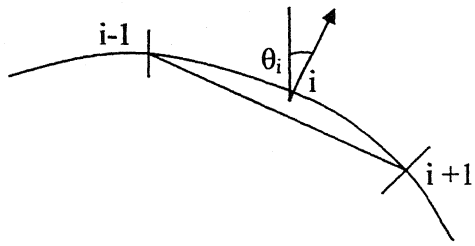

Fig. D.1: Positive Curvature at node i

$$\bar{t} = (D_s \delta_s \Omega \gamma_s t)/(kTW^4), \bar{s} = s/W, \bar{x} = x/W, \tag{D.4}$$

$$\bar{a} = a/W, \tag{D.5}$$

$$\bar{v}_n = v_n kTW^3/(D_s \delta_s \Omega \gamma_s), \tag{D.6}$$

and,

$$\bar{\sigma}_\infty = \sigma_\infty W/\gamma_s, \tag{D.7}$$

The non-dimensional form used in the present simulation are given by

$$\bar{v}_n = \partial^2 \bar{x}/\partial \bar{s}^2 \tag{D.8}$$

$$\cos\psi = \gamma_b/(2\gamma_s) \tag{D.9}$$

$$\kappa_{tip} = \bar{\sigma}_\infty K_1 - (2/3)(1-\bar{a})F(\partial \bar{x}/\partial \bar{s})_{tip} \tag{D.10}$$

The non-dimensional normal velocity of atoms at each node, $\bar{v}_i$, can be calculated by

$$\bar{v}_i = [(\bar{\kappa}_{i+1} - \bar{\kappa}_i)/\bar{s}_{i+1} - (\bar{\kappa}_i - \bar{\kappa}_{i-1})/\bar{s}_i]/[(\bar{s}_{i+1} + \bar{s}_i)/2] \tag{D.11}$$

where, $\bar{s}_i$ is the non-dimensional distance between points "i-1" and "i". Consequently, the new coordinates of node points $(\bar{x}_i', \bar{y}_i')$ are determined by

$$(\bar{x}_i', \bar{y}_i') = (\bar{x}_i + \Delta\bar{t}\,\bar{v}_i \sin\theta_i, \bar{y} + \Delta\bar{t}\,\bar{v}_i \cos\theta_i) \tag{D.12}$$

$$\theta_i = \tan^{-1}\left(-(\bar{y}_{i+1} - \bar{y}_{i-1})/(\bar{x}_{i+1} - \bar{x}_{i-1})\right) \tag{D.13}$$

where, $(\bar{x}_i, \bar{y}_i)$ are the old coordinates and $\Delta\bar{t}$ is the non-dimensional time increment. The increment of displacement, $\Delta\bar{t}\,\bar{v}_i$, is kept below 0.001 at all nodes for minimizing the error. The new coordinates at the groove tip are obtained by,

$$\begin{aligned} \bar{x}_N' &= \bar{x}_{N-1}' + \bar{y}_{N-1}'/\tan\psi \\ \bar{y}_N' &= 0 \end{aligned} \tag{D.14}$$

An additional node is introduced at the midpoint of the element when the distance between the two end nodes exceeds twice the initial spacing. The curvature at the additional node is taken to be the average of the curvatures at the two neighboring nodes. Repeating the above procedure, the grooving process can be fully simulated. This is similar to simulation conducted on the cavity growth in the creep by Martinez and Nix [5].